An Operational Thermodynamic-Dynamic Model for the Coastal Labrador Sea Ice Melt Season: Labrador Coastal Ice Melt and Dynamics Model (Version 1)

Ian D. Turnbull[1], and Rocky S. Taylor[1,2]

[1]C-CORE

[2]Memorial University of Newfoundland (MUN)

Corresponding author: Ian Turnbull (ian.turnbull@card-arctic.ca)

1 C-CORE
Captain Robert A. Bartlett Building
1 Morrissey Road
St. John's, Newfoundland and Labrador A1B 3X5 Canada
Ian Turnbull Phone: (709)-864-6208
Fax: (709)-864-4706

2 Memorial University of Newfoundland
Faculty of Engineering and Applied Science
S.J. Carew Building
240 Prince Philip Drive
St. John's, Newfoundland and Labrador A1B 3X5 Canada
Rocky Taylor Phone: (709)-864-4370
Fax: (709)-864-4706
E-mail: rocky.taylor@card-arctic.ca

Abstract

An offshore operations thermodynamic-dynamic prediction model of sea ice break-up and drift is presented for central coastal Labrador in Atlantic Canada, and demonstrated for portions of the 2015 spring break-up of the land-fast ice. The model validation is performed using the data from ice tracking buoys deployed on the land-fast ice, which began drifting after break-up of the land-fast ice. The model uses a one-dimensional thermodynamic parameterization for ice melt and growth, includes snow accumulation and melt, and melt-pond and lead growth and contraction. The dynamic model uses a Smoothed Particle Hydrodynamics (SPH) parameterization for ice motion and changes in ice thickness and concentration. The dynamic forcing parameters include wind and ocean current drag, Coriolis deflection, internal ice stresses, and gravitational forcing due to sea surface gradients. A coastal repulsion force is employed to prevent ice particles from crossing the coastal boundaries. The model is sensitive to the prescribed initial snow depth on the sea ice. In the present work, analysis of results is focused on the offshore regions of Makkovik and Nain, Labrador. The melt of the coastal land-fast ice in these regions can be adequately simulated by the thermodynamic model alone. The model predicts the timing of the local land-fast ice break-up to within 4.6 hours to six days, and can simulate observed ice buoy drift speeds to within 1.5 meters per second.

1 Introduction

Sea ice forecast models are an important tool for offshore industries operating in ice-prone environments, such as those involved in hydrocarbon exploration and development or marine transport. Accurate pack ice model forecasts allow for operations to be planned for maximum safety, efficiency, and minimum downtime as operators make the best possible preparations for the anticipated ice conditions, and can develop an advance understanding of how those conditions and associated hazards are likely to evolve during operations. While small-scale models are useful for generating drift forecasts for single or several ice floes over spatial scales of up to tens of km, regional and basin-scale models provide forecasts of ice conditions on scales of tens to hundreds of km, and permit operators to develop a picture of changes in ice conditions over such a broad area in which vessels and drilling platforms may travel. Such forecast models are useful for generating ice forecasts on timescales of days to months.

In this paper, a model is presented to simulate the melt and break-up of the land-fast ice along the central Labrador coast during the spring break-up season, as well as the regional ice dynamics in the further offshore marginal ice zone (MIZ). The model is designed to be an operational planning and ice forecast tool for the offshore oil and gas industry, as well as the marine transport industry. It is designed to accept gridded metocean input parameters from numerical weather prediction and ocean models. The model simulations presented here are run for selected periods during April-May 2015, and are compared to in-situ observations of ice drift as recorded by tracking buoys deployed on ice floes, and to reanalysis data on ice thickness, concentration, and velocity as provided by the Operational Mercator global Ocean analysis and forecast system. The models runs are forced with atmospheric and precipitation reanalysis data from the North American Regional Reanalysis (NARR), the European Center for Medium Range Weather Forecasting (ECMWF), and with ocean model output from the Operational Mercator global Ocean analysis and forecast system.

The results presented here focus particularly on the regions offshore Makkovik and Nain, Labrador, as these locations have been identified as economically important for vessel transit. Makkovik has been identified as a potential landing site for a pipeline from oil and gas fields offshore Labrador, and Nain is located near the port of Edward's Cove which serves the Voisey's Bay nickel mine (Vale, 2015). In this paper, two locations offshore Makkovik and Nain are selected to demonstrate the thermodynamic model simulation of the melt and break-up of the land-fast ice during April 1 – May 31, 2015. Results from the thermodynamic model are also presented for the central coastal Labrador region from Makkovik to Nain. Subsequently, the coupled thermodynamic-dynamic model is demonstrated for the Makkovik-Nain region for May 1-7, 2015, which coincides with the break-up of the land-fast ice offshore Nain.

1.1 Ice tracking buoy deployments

On April 9, 2015, six Iridium satellite-tracked buoys were deployed toward the outer edge of the land-fast ice offshore Labrador (see Figure 1). The buoys were dropped out of a Twin Otter fixed-wing airplane, and were deployed in two triangular arrays offshore Makkovik and Nain. These buoy deployments served to collect data on the precise timing of the land-fast ice break-up at these locations during the 2015 melt season, and the subsequent drift patterns of the broken floes. Table 1 summarizes the offshore deployment areas for the six buoys and the time periods over which they drifted on ice following the break-up of the land-fast ice on which they were deployed. The on-ice drift periods were determined from analysis of the internal temperatures transmitted by the buoys, as the on-ice periods were characterized by distinctly larger diurnal temperature fluctuations in response to air temperatures, compared with more homogeneous temperature records once the buoys fell into open water. The open water drift of the buoys is not considered in this paper.

Buoys 1, 4, and 6 were deployed offshore Nain, and buoys 2, 3, and 5 were dropped offshore Makkovik. The first drift motion recorded by the buoys took place on April 23 offshore Makkovik, and on May 1 offshore Nain. Buoy 5 failed on May 28 on the land-fast ice offshore Makkovik and never recorded any movement (Table 1).

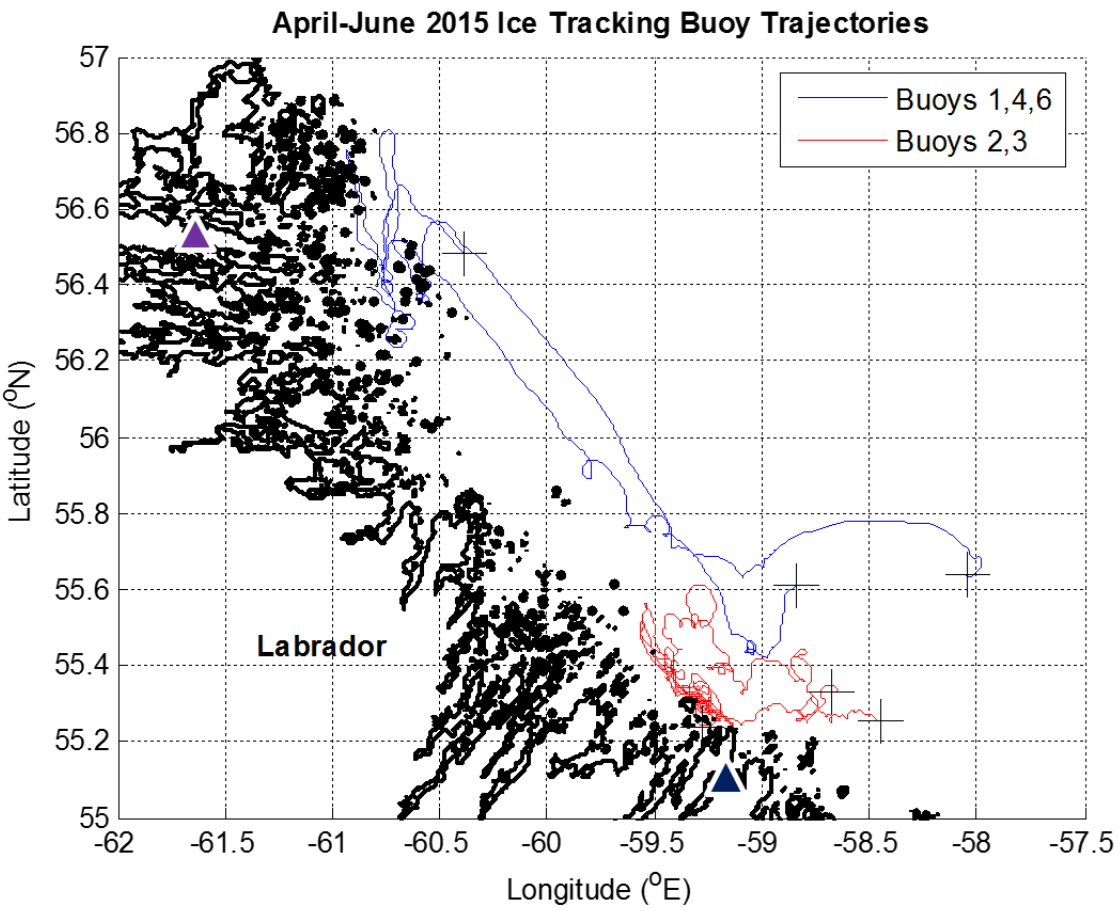

Figure 1. Trajectories of six ice tracking buoys offshore Labrador during April 23 – June 12, 2015. The dark blue and purple white-outlined triangles mark the locations of Makkovik and Nain, respectively. The black plus (+) symbols mark the ends of the buoys' on-ice drift trajectories.

Table 1. Deployment areas and time periods over which the six ice buoys drifted on ice following the break-up of the land-fast ice.

Buoy	Deployment Area	Ice Drift Period
1	Nain	May 1-18
2	Makkovik	April 23 – June 12
3	Makkovik	April 23 - June 8
4	Nain	May 2-11
5	Makkovik	N/A
6	Nain	May 6-19

1.2 Regional environment

Coastal Labrador is dominated by the Labrador Current, which has a mean surface speed of 0.25-0.5 m s^{-1} (Lazier and Wright, 1993) toward the south and SSE, parallel to the coast (Figure 2).

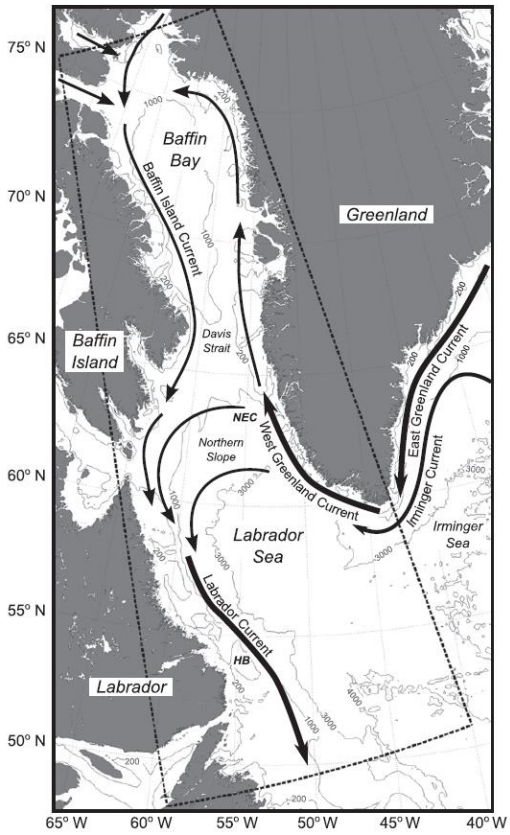

Figure 2. Mean surface currents offshore Labrador flow parallel to the coast toward the south and SSE at speeds of 0.25-0.5 m s^{-1} (image reproduced from Fenty and Heimbach, 2013).

Freeze-up along the Labrador coast typically begins in December, with land-fast ice forming from the northern edge of Labrador to just south of Lake Melville (Canadian Coast Guard, 2013). By April 1st, a large region of 9+/10ths mainly first-year (FY) ice has formed further offshore from the land-fast ice and drifts southward with the Labrador Current, being replenished by more northerly-sourced ice from Baffin Bay (Figure 3). The boundary between the regions of 9+/10ths pack ice and open water is typically sharp and along the edge of the Labrador Shelf (see Figure 5) near the western edge of the Labrador Current (Yao et al., 2000b), with only a thin band of ice 1-8/10ths in concentration along the boundary (Figure 3).

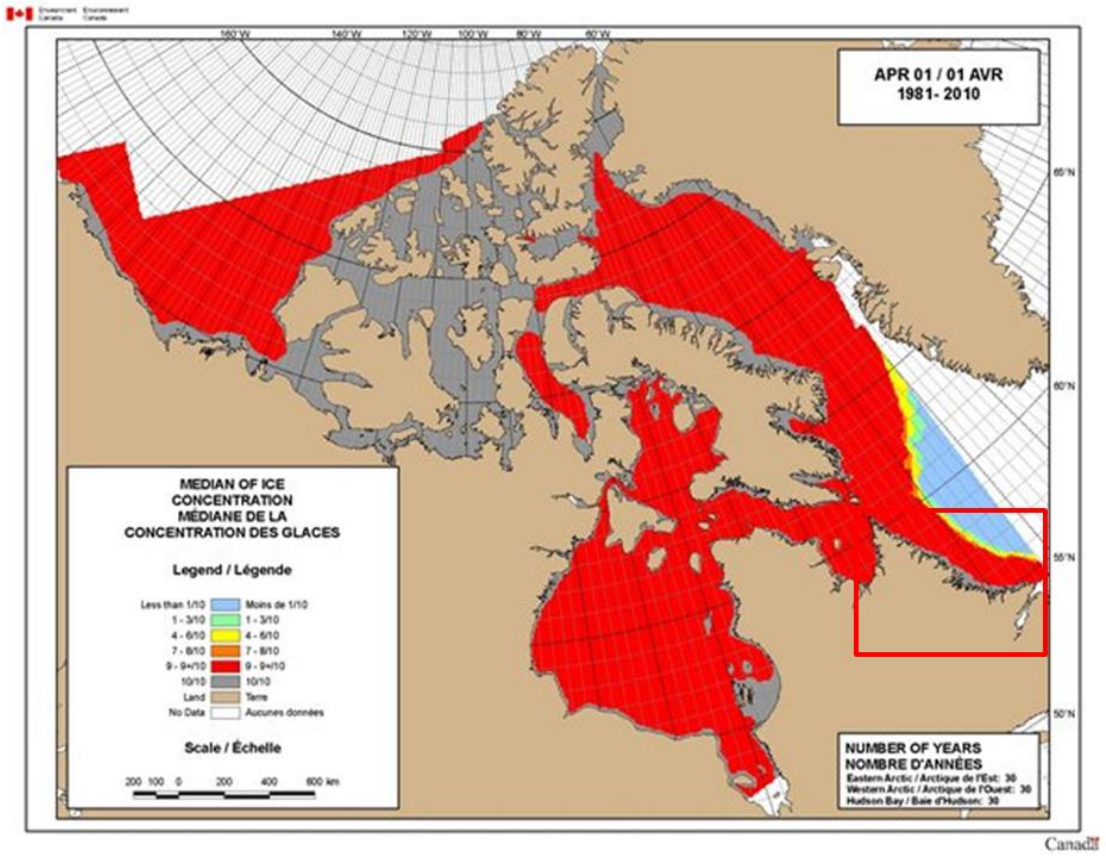

Figure 3. Maximum spring ice cover offshore Labrador (red-boxed region) typically includes a band of 10/10ths land-fast ice (gray region), and a more extensive zone of dynamic pack ice 9+/10ths in concentration (red region) further offshore (Canadian Coast Guard, 2013).

The onset of break-up of the high-concentration ice along the coast of Labrador typically occurs in mid-June for most of the region, with break-up commencing in early July for the most northerly areas (Figure 4).

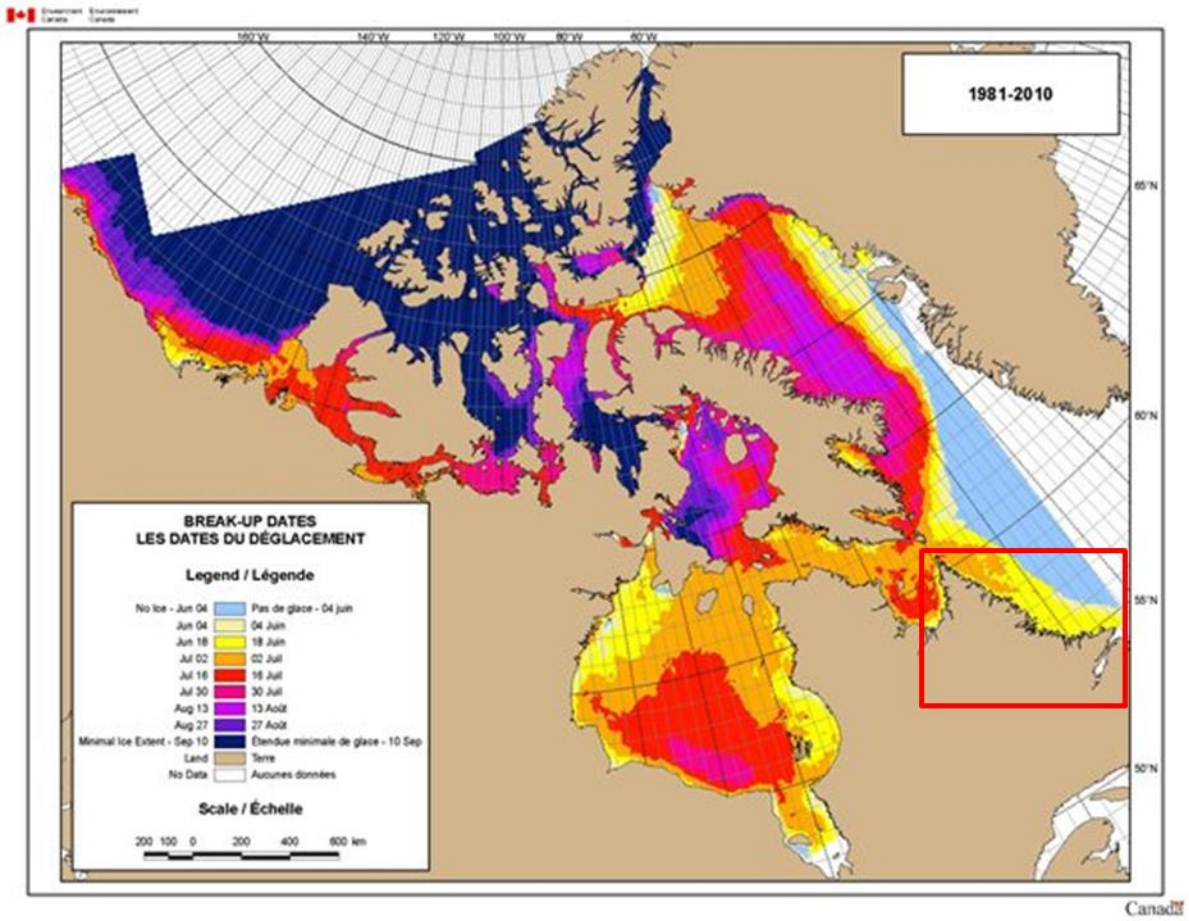

Figure 4. The onset of pack ice break-up in the offshore Labrador region (red-boxed region) typically occurs in mid-June to early July (Canadian Coast Guard, 2013).

The water depth offshore Labrador extends to approximately 500 m along the Labrador Shelf, with a few pockets as deep as about 1000 m (Figure 5). Further offshore, the depth rapidly increases to greater than 2000 m. At its maximum seasonal extent in March-April, sea ice typically extends to the shelf break front (Yao et al., 2000b) along the 500 m depth contour.

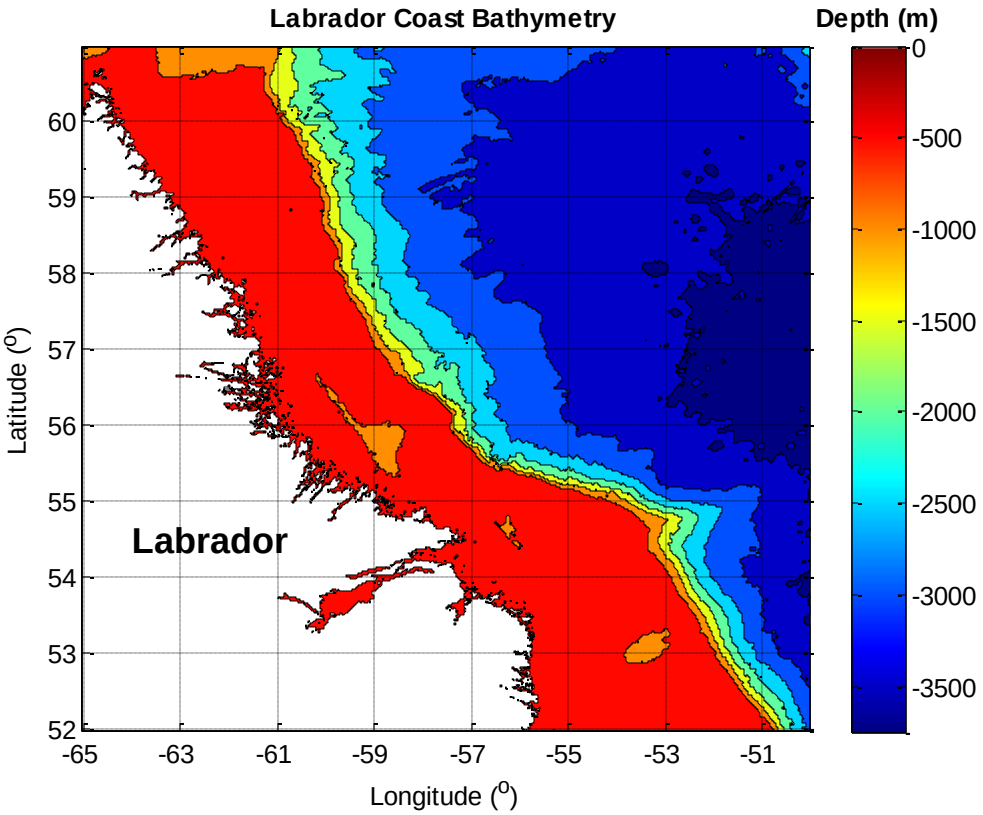

Figure 5. The bathymetry offshore Labrador (General Bathymetric Chart of the Oceans, GEBCO, 2008, 30-second data).

2 Ice Environmental Modeling

2.1 Previous modeling studies

Existing modelling studies for the offshore Labrador ice environment tend to focus on seasonal to inter-annual sea ice variability and its interaction with oceanic mixing and convection. Few studies have presented efforts to develop operational ice forecast models for the region.

A study by Peng, 1989, for example, applies a coupled ice-ocean model to simulate ice growth and transport in the Labrador Sea over a single winter season.

Prinsenberg and Yao, 1999 presents a climatological study of the seasonal evolution of sea ice cover offshore eastern Canada for 1991-1992 using a three-dimensional coupled ice-ocean model. The study additionally presents model simulations of ice cover under a scenario of a doubling of atmospheric carbon dioxide concentration by using as input the expected atmospheric conditions under such a scenario.

A paper by Yao, 2000 focuses on the assimilation of satellite-derived sea surface temperature (SST) data into a coupled ice-ocean model for the Labrador Sea, with the primary objective of improving the modelled location of the ice edge. The SST data assimilation, however, did not improve model performance in this regard.

A study by Yao et al., 2000a focuses on verification of a coupled ice-ocean model for the Newfoundland shelf during February-April 1997, with the region of interest (ROI) stretching from offshore central-northern Newfoundland to southern Labrador. The model output was compared in particular to observed ice edge location, southern ice extent, and ice thickness as derived from Canadian Ice Service (CIS) charts, and to ice drift velocities as measured by satellite-tracked ice buoys.

Yao et al., 2000b presents results of a modelling study of the seasonal variation of sea ice in the Labrador Sea using an ice model coupled to the Princeton ocean model. In this paper, the Princeton ocean model is forced by monthly climatological atmospheric data.

A paper by Sayed et al., 2002 presents the operational ice dynamics model developed by CIS for ice forecasting in regional environments. The model uses a Lagrangian Particle-In-Cell (PIC) approach to model ice advection. In the paper, a seasonal simulation of the model is presented, with the ice model coupled to the Princeton ocean model. The model output is compared with the measured trajectory of a single ice tracking beacon offshore Labrador during January-April 1999, and with the January-May 1999 evolution of the total ice area and mean thickness over a large area encompassing the east coast of Canada.

A study by Fenty and Heimbach, 2013 explores the relationship between sea ice and oceanic variability in the Labrador Sea and Baffin Bay. It analyzes the response of the annual sea ice cover variability to ocean currents and water mass mixing and convection in the region.

A paper by Cooke et al., 2014 presents a study of inter-annual sea ice variability in the western Labrador Sea using a coupled sea ice-ocean model. The paper focuses on the relationships between sea ice concentration and the underlying water column properties in terms of temperature, salinity, and convection. Cooke et al., 2014 use the Nucleus for European Modelling of the Ocean (NEMO) model and couple it to the Louvain Sea Ice Model 2 (LIM2) multi-layered sea ice model. Atmospheric forcing is provided by the National Center for Environmental Prediction/National Center for Atmospheric Research (NCEP/NCAR) six-hourly reanalysis data from 1948-2005.

2.2 Thermodynamic model description

The model presented in this paper was developed in the programming language of MATLAB. The thermodynamic model is largely based on the one-dimensional model presented in Ebert and Curry, 1993 (hereafter referred to as EC93), which is in turn based on the model presented in Maykut and Untersteiner, 1971. The thermodynamic model can be run as a standalone model, or can be coupled to the dynamic ice model. The thermodynamic model accounts for heat fluxes from the surface ocean through the ice slab, heat exchanges with the surface air or snow layer if present, snow layer accumulation, melt, and heat exchange with the ice and atmosphere, incoming shortwave (solar) radiation, total cloud cover and its effects on atmospheric albedo and down-welling longwave radiation, and lead and melt pond growth and contraction. The thermodynamic model-only runs are initialized with ice particles on a

grid with 0.45° spacing (approximately 50 km). Ice particles are dropped from the model grid once they have completely melted away.

2.2.1 Ice and snow thermal properties and heat conduction

In the thermodynamic model, the sea ice vertical temperature profile and thickness are governed by the one-dimensional heat equation as per EC93,

$$(\rho c)_i \left(\frac{\partial T_i}{\partial t}\right) = k_i \left(\frac{\partial^2 T_i}{\partial z^2}\right) = \frac{\partial F_c}{\partial z}, \quad (1)$$

where $(\rho c)_i$ is the volumetric heat capacity of ice, T_i is ice temperature (K), t is time (seconds), k_i is the thermal conductivity of ice, F_c is the upward conductive flux (W m^{-2}), and z is the depth level in the ice slab (m) with $z = 0$ defined at the ice surface. As the heat capacity and thermal conductivity of ice are affected by its temperature and salinity, the volumetric heat capacity of the sea ice (J m^{-3} K^{-1}) is defined as (*e.g.*, EC93),

$$(\rho c)_i = (\rho c)_{i,f} + \frac{\gamma S_i}{(T_i - 273)^2}, \quad (2)$$

where $(\rho c)_{i,f}$ is the volumetric heat capacity of pure ice (1.883x10^6 J m^{-3} K^{-1}) and γ is a constant (1.715×10^7 J K m^{-3} ppt^{-1}), and S_i is the ice salinity (ppt). The ice thermal conductivity (W m^{-1} K^{-1}) is defined as (*e.g.*, EC93),

$$k_i = k_{i,f} + \frac{\mathrm{B} S_i}{T_i - 273}, \quad (3)$$

where $k_{i,f}$ is the thermal conductivity of pure ice (2.034 W m^{-1} K^{-1}), and B is a constant (0.1172 W m^{-1} ppt^{-1}). As per EC93, T_i is constrained to values 272.9K or less in order to avoid a singularity at 273K in Eqs. (2) and (3). The ice salinity (ppt) is approximated by the equation from Timco and Johnston, 2002 for cold FY ice as a function of thickness, *e.g.*,

$$S_i = 13.4 - 17.4 h_i \quad \text{for } h_i \leq 0.34\text{m}, \quad (4)$$

$$S_i = 8.0 - 1.62 h_i \quad \text{for } h_i > 0.34\text{m}, \quad (4)$$

where h_i is ice thickness (m).

The ice temperature profile is initialized with a linear trend between the boundary conditions set at the ice base and surface. The ice basal temperature is fixed at the melting point of seawater, and the ice surface temperature is calculated as a function of the surface (2m) air temperature. The ice temperature is calculated at four evenly-spaced points in the vertical slab, including the boundaries at the ice-water and ice-snow or ice-air (when no snow is present) interfaces.

The snow-free ice surface temperature is calculated as a function of the surface air temperature according to the function (*e.g.*, Timco and Frederking, 1990),

$$T_{i,s} = T_a \quad \text{for } -2 \geq T_a \geq -10,$$

$$T_{i,s} = 0.6 T_a - 4 \quad \text{for } T_a < -10,$$

$$T_{i,s} = -2.0 \quad \text{for } T_a > -2, \tag{5}$$

where $T_{i,s}$ is the ice surface temperature (°C), and T_a is the 2 m air temperature (°C). When the air temperature is higher than -2°C, the ice surface temperature is assumed to be at the approximate freezing point of saline FY sea ice, -2°C.

The basal ice temperature is calculated as the freezing temperature of seawater as a function of sea surface salinity (*e.g.*, Fofonoff and Millard Jr., 1983),

$$T_{o,f} = -5.33x10^{-7}S^3 - 9.37x10^{-6}S^2 - 0.0592S, \tag{6}$$

where $T_{o,f}$ is the freezing temperature of seawater (°C), and S is the sea surface salinity (ppt).

When a snow layer is present on the sea ice, the snow vertical temperature profile is governed by a similar one-dimensional heat equation as that used for sea ice (*e.g.*, EC93),

$$(\rho c)_s \left(\frac{\partial T_s}{\partial t}\right) = k_s \left(\frac{\partial^2 T_s}{\partial z^2}\right) = \frac{\partial F_c}{\partial z}, \tag{7}$$

where $(\rho c)_s$ is the volumetric heat capacity of snow, T_s is the snow temperature (K), k_s is the thermal conductivity of snow, and z is again defined with $z = 0$ at the snow surface. The snow temperature is calculated at three evenly-spaced points in the vertical slab, including the boundaries at the snow-ice and snow-air interfaces. The volumetric heat capacity of snow is given by (*e.g.*, EC93),

$$(\rho c)_s = \rho_s(92.88 + 7.364T_s), \tag{8}$$

where ρ_s is the density of the snow layer (kg m^{-3}) on the sea ice. The value of ρ_s is 330 kg m^{-3} if the surface air temperature is less than 0°C, and is 450 kg m^{-3} if the surface air temperature is 0°C or greater (EC93). Compaction of the snow layer due to fresh snowfall and time is neglected in the present model. The snow thermal conductivity is given by (*e.g.*, EC93),

$$k_s = 2.845 \times 10^{-6}\rho_s^2 + 2.7 \times 10^{-4} \times 2^{\frac{T_s - 233}{5}}. \tag{9}$$

The temperature at the snow-ice interface is computed from Eq. (7) and is set to the ice surface temperature. The temperature at the snow-air interface is initialized in K by (*e.g.*, Tonboe et al., 2011),

$$T_{s,top} = 1.14T_a - 37.94 \quad \text{for } T_a < 273.15,$$

$$T_{s,top} = 273.15 \quad \text{for } T_a \geq 273.15. \tag{10}$$

Snow temperatures are constrained to 0°C and below. The effect of sea water flooding on the snow surface is neglected in this model. As with the vertical ice temperature profiles, at the start of each model run, the vertical snow temperatures are initialized with linear vertical profiles. From the second time-step forward, the temperature at the snow or snow-free ice surface is solved using the net surface heat flux (see Eq. 49 in section 2.2.7).

2.2.2 Solar radiation

The incoming solar (shortwave) radiation (W m^{-2}) at the top of the atmosphere is given by (*e.g.*, FAO, 2015),

$$F_{SW} = \frac{12 S_o d_r \left((\omega_2 - \omega_1) \sin(\phi) \sin(\lambda) + \cos(\phi) \cos(\lambda) (\sin(\omega_2) - \sin(\omega_1)) \right)}{\pi}, \quad (11)$$

where S_o is the solar constant (1365.5 W m^{-2}), d_r is the inverse relative Earth-Sun distance (radians), ω_1 and ω_2 are the solar time angles (radians) immediately before and after a given time-step, respectively, ϕ is the latitude (radians), and λ is the solar declination (radians). The inverse relative Earth-Sun distance is defined by (*e.g.*, FAO, 2015),

$$d_r = 1 + 0.033 \cos\left(\frac{2\pi J}{365}\right), \quad (12)$$

where J is the Julian date. The solar declination is defined by (*e.g.*, FAO, 2015),

$$\lambda = 0.409 \sin\left(\frac{2\pi J}{365} - 1.39\right). \quad (13)$$

The solar time angles are given by (*e.g.*, FAO, 2015),

$$\omega_1 = \omega - \frac{\pi dt}{24},$$

$$\omega_2 = \omega + \frac{\pi dt}{24}, \quad (14)$$

where ω is the solar time angle (radians) at the midpoint of the period over which the incoming solar radiation is calculated, and dt is the length of the calculation period (hours). The solar time angle at the midpoint of the period is defined by (*e.g.*, FAO, 2015),

$$\omega = \frac{\pi\left((t + 0.06667(L_z - L_m) + S_c) - 12 \right)}{12}, \quad (15)$$

where t is the standard clock time at the hour midpoint (*e.g.*, $t = 13.5$ if the calculation time is between 13:00 and 14:00 hours), L_z is the longitude of the center of the local time zone (60°W for the Atlantic Standard Time or AST zone) in degrees west of Greenwich, L_m is the longitude of the calculation site in degrees west of Greenwich, and S_c is the seasonal correction for solar time (hours). The solar time seasonal correction is given by (*e.g.*, FAO, 2015),

$$S_c = 0.1645 \sin(2b) - 0.1255 \cos(b) - 0.025 \sin(b), \quad (16)$$

where b is defined as $\frac{2\pi(J-81)}{364}$ (FAO, 2015).

Finally, the sunset hour angle ω_s (radians) is used to determine whether or not the sun is below the horizon at a given time. The sunset hour angle is defined as (*e.g.*, FAO, 2015),

$$\omega_s = \text{acos}(-tan(\phi)\, tan(\lambda)). \quad (17)$$

The sun is below the horizon when $\omega < -\omega_s$ or $\omega > \omega_s$ and $F_{SW} = 0$. Note that times used to calculate F_{SW} are local times for AST, which is UTC-3:00 during April-May.

The flux of solar radiation (W m^{-2}) which penetrates the snow-free ice surface as a function of depth in the ice, z (m), is governed by Beer's Law (*e.g.*, EC93),

$$F_{i0}(z) = I_0(1-\alpha_i)F_{SW}e^{-\kappa_i(z)}, \quad (18)$$

where I_0 is the fraction of solar radiation which penetrates the atmosphere, α_i is the ice albedo, and κ_i is the bulk shortwave extinction coefficient for sea ice (1.5 m^{-1}). The fraction of solar radiation penetrating the atmosphere is defined by (*e.g.*, EC93),

$$I_0 = 0.18(1-T_{cc}) + 0.35T_{cc}, \quad (19)$$

where T_{cc} is the total fractional cloud cover. If there is snow on the sea ice, then Eq. (18) becomes,

$$F_{i0}(z) = (1-\alpha_i)F_{i0,s}e^{-\kappa_i(z)}, \quad (20)$$

where $F_{i0,s}$ is the fraction of solar radiation which penetrates the snow layer. The fraction of solar radiation penetrating the snow layer is given by,

$$F_{i0,s} = I_0(1-\alpha_s)F_{SW}e^{-\kappa_s(z)}, \quad (21)$$

where α_s is the snow albedo, κ_s is the bulk shortwave extinction coefficient for snow (0.42 m^{-1} as per Davis, 1996), and z (m) is the depth in the snow layer. The fractions of penetrating solar radiation determined from Eqs. (18) and (21) are used to update the ice and snow temperature profiles as computed from Eqs. (1) and (7), respectively. In Eqs. (1) and (7), the quantity F_c is replaced with F_{i0} and $F_{i0,s}$, respectively.

2.2.3 Meltwater ponds

The model presented here allows for the growth and contraction of meltwater ponds on the surface of the sea ice in terms of the depth and fractional area coverage of the ponds. The rate of meltwater pond depth change (m s^{-1}) is defined by (*e.g.*, EC93 and Holland et al., 2012),

$$\frac{\partial h_p}{\partial t} = \left(\left(1-A_{pond}\right)\left(\frac{\partial h_i}{\partial t}\right)_0 + \frac{A_{pond}F_p}{L_{fi}} + RF + \frac{SF\rho_s}{\rho_w}\right)(1-r), \quad (22)$$

where h_p is pond depth (m), A_{pond} is pond fractional area, $\left(\frac{\partial h_i}{\partial t}\right)_0$ is the rate of ice melt at the top surface of the sea ice (m s^{-1}), F_p is the solar radiation flux (W m^{-2}) which is absorbed by both the pond water and the underlying sea ice, L_{fi} is the latent heat of fusion of sea ice (3.014×10^8 J m^{-3}), RF and SF are rainfall and snowfall, respectively (m s^{-1}), ρ_w is the density of melt-pond water (1000 kg m^{-3}), and r is the fraction of surface meltwater and rainfall which runs off the ice surface while the rest remains in the ponds. The quantity r is defined as $0.85 - 0.7A_{ice}$ (Holland et al., 2012), where A_{ice} is the fractional ice area concentration of a given model particle. As per EC93, once the melt-pond depth on a given model particle is greater than zero, the melt-pond fractional area is initialized at 0.10.

The flux of solar radiation absorbed by the pond water and sea ice is defined by (*e.g.*, EC93),

$$F_p = F_{SW}\left(a_p + a_p\alpha_i t_p + t_p(1-\alpha_i)(1-I_0)\right)(1-\alpha_p), \quad (23)$$

where a_p is the pond absorption coefficient ($1 - t_p^{0.89}$), t_p is the pond transmissivity ($0.36 - 0.17\log_{10}(h_p)$), and α_p is the pond albedo. As per EC93, the maximum allowed melt-pond depth is set to 0.8 m. Any melt-ponds which grow to a depth greater than the ice thickness (when the ice thickness is less than 0.8 m) are subsequently treated as leads in the ice pack (see subsection 2.2.4).

One melt ponds have begun to form, the melt-pond fractional area is computed iteratively using the scheme of Holland et al., 2012 which allows for growth and contraction of the ponds based on the ice surface temperature. The evolution of the melt-pond fractional area in terms of growth and contraction is defined respectively as follows,

$$A_{pond(i+1)} = A_{pond(i)} + \frac{(1-r)\left(\left(\frac{\partial h_i}{\partial t}\right)_0\left(\frac{\rho_i}{\rho_w}\right)+RF\right)}{h_p}dt \qquad \text{for } T_{i,s} > -2°C,$$

$$A_{pond(i+1)} = A_{pond(i)}e^{\frac{0.01\left(T_{i,s}+2\right)}{2}} \qquad \text{for } T_{i,s} \leq -2°C, \tag{24}$$

where i is the model time-step index, and dt is the model time-step (seconds). As per EC93, the melt-pond fractional area is restricted to a maximum value of 0.25. Melt-ponds are not permitted to form until all of the snow has melted from a model particle.

2.2.4 Lead development and ocean heat fluxes

The present model uses the parameterizations of EC93 to simulate the ocean-air and ocean-ice heat exchanges and the development of leads in the ice pack. The net heat flux (W m^{-2}) at the lead surface is defined by (*e.g.*, EC93),

$$F_{lead} = \epsilon_w F_{LW} - \epsilon_w \sigma T_w^4 + (1-\alpha_w)(1-i_w)F_{SW} - F_{sens,w} - F_{lat,w}, \tag{25}$$

where $\epsilon_w$is the emissivity of water (0.97), F_{LW} is the incoming (downward) infrared heat flux from the atmosphere (W m^{-2}), σ is the Stefan-Boltzmann constant (5.67×10^{-8} W m^{-2} K^{-4}), T_w is the surface ocean temperature (K), α_w is the surface ocean albedo, i_w is the fraction of solar radiation transmitted through the surface water layer equivalent in depth to the ice thickness and not absorbed, and $F_{sens,w}$ and $F_{lat,w}$ are the sensible and latent heat fluxes from the ocean surface layer, respectively (W m^{-2}). The parameter i_w is defined as follows (*e.g.*, EC93),

$$i_w = 1 - \frac{(a_1 + a_2\ln(h_i))}{1-\alpha_w}, \tag{26}$$

where $a_1 = 0.5676$ and $a_2 = 0.1046$ under clear-sky conditions and $a_1 = 0.3938$ and $a_2 = 0.1208$ under cloudy-sky conditions. In the present model, conditions are considered to be clear-sky if the total cloud area fraction is less than 0.35.

The growth of the fractional lead area is defined by (*e.g.*, EC93),

$$\frac{\partial A_{lead}}{\partial t} = \frac{A_{lead}F_{lead}}{L_{fi}h_i + L_{fs}h_s}, \tag{27}$$

where L_{fs} is the latent heat of fusion of snow (1.097×10^8 J m^{-3}), and h_s is the thickness of the snow layer on the ice (m).

The expression for the solar radiation flux (Wm^{-2}) absorbed beneath the ice is represented as the sum of the solar flux through the leads and the solar radiation transmitted through snow-free ice and is given as follows (*e.g.*, EC93),

$$F_{wi} = A_{lead}(1-\alpha_w)i_w F_{SW} + (1-A_{lead})(1-\alpha_i)I_0 e^{-\kappa_i h_i} F_{SW}. \quad (28)$$

The water temperature immediately beneath the ice, T_{wi}, is governed by (*e.g.*, EC93),

$$\frac{\partial T_{wi}}{\partial t} = \frac{F_{wi}-(1-A_{lead})F_b}{\left(d_w-\left(\frac{\rho_i}{\rho_w}\right)h_i\right)(\rho c)_w}, \quad (29)$$

where F_b is the heat flux at the base of the ice (W m^{-2}), d_w is the ocean mixed layer depth (m), and $(\rho c)_w$ is the volumetric heat capacity of water (4.19×10^6 J m^{-3} K^{-1}). In deeper water, the ocean mixed layer depth is assumed to be 30 m (EC93), and is assumed to be the bathymetric water depth in shallower water less than 30 m deep (see Figure 5). The model is initialized with $T_{wi} = T_{o,f}$ as per Eq. (6). The heat flux at the base of the ice is given by (*e.g.*, EC93),

$$F_b = (\rho c)_w C_{Tb}\left(T_{wi} - T_{o,f}\right), \quad (30)$$

where C_{Tb} is the bulk transfer coefficient. As per EC93, C_{Tb} is defined as,

$$C_{Tb} = 1.26\times10^{-4} h_i^{-0.5} \quad \text{for } h_i < 3 \text{ m},$$

$$C_{Tb} = 7.27\times10^{-5} \quad \text{for } h_i \geq 3 \text{ m}. \quad (31)$$

2.2.5 Atmospheric properties and heat fluxes

The ocean and ice atmospheric heat fluxes in the present model are defined by the bulk aerodynamic formulae for sensible, latent, and longwave radiative heat transfer as per EC93. The sensible heat flux over ice (W m^{-2}) is defined as (*e.g.*, EC93),

$$F_{sens,i} = \rho_a c_{pa} C_{Ti} U_a (T_{i,s} - T_a), \quad (32)$$

where ρ_a is the air density (kg m^{-3}) at 2 m, c_{pa} is the specific heat of air at constant pressure (J kg^{-1} K^{-1}), C_{Ti} is the bulk heat and moisture transfer coefficient over ice, and U_a is the wind speed at 2 m (m s^{-1}). The air density is computed according to the ideal gas law as (*e.g.*, Tsonis, 2002),

$$\rho_a = \frac{P_s}{RT_a}, \quad (33)$$

where P_s is the surface or sea level atmospheric pressure (Pa), R is the gas constant for air (J kg^{-1} K^{-1}), and the 2 m air temperature T_a is in K. The gas constant for air depends on the air specific humidity as follows (*e.g.*, Tsonis, 2002),

$$R = R_d(1 + 0.61 q_a), \quad (34)$$

where R_d is the gas constant for dry air (278.058 J kg^{-1} K^{-1}), and q_a is the specific humidity of the air at 2 m. The air specific humidity is defined by (*e.g.*, Tsonis, 2002),

$$q_a = \frac{\frac{0.622 e_w}{P_s - e_w}}{1+\left(\frac{0.622 e_w}{P_s - e_w}\right)}, \quad (35)$$

where e_w is the vapor pressure in the air (Pa) at 2 m. The vapor pressure is equivalent to $(RH)(e_{sw})$, where RH is the relative humidity at 2 m, and e_{sw} is the saturation vapor pressure (Pa) at 2 m. The saturation vapor pressure is given by (*e.g.*, Tsonis, 2002),

$$e_{sw} = 611 e^{19.83 - \frac{5417}{T_a}}, \quad (36)$$

where T_a is in K. The specific heat of air at constant pressure is defined as $\frac{7}{2}R$ (Tsonis, 2002). The bulk heat and moisture transfer coefficient over ice is defined as (*e.g.*, EC93),

$$C_{Ti} = C_{T0i}\left(1 - \frac{2 b_a Ri_{ice}}{1 + c|Ri_{ice}|^{0.5}}\right) \quad \text{for } Ri_{ice} < 0,$$

$$C_{Ti} = C_{T0i}(1 + b_a Ri_{ice})^{-2} \quad \text{for } Ri_{ice} \geq 0, \quad (37)$$

where C_{T0i} is a heat and moisture transfer coefficient for a neutral surface layer over ice (1.3×10^{-3}), b_a is a parameter for atmospheric turbulence equal to 20, Ri_{ice} is the bulk Richardson number over ice, and c has a value of $(1961 b_a C_{T0i})$ for an ice roughness length of 1.6×10^{-4} m. The Richardson number is defined as (*e.g.*, EC93),

$$Ri_{ice} = \frac{g(T_a - T_{i,s})\Delta z}{T_a U_a^2}, \quad (38)$$

where g is the earth gravitational acceleration (9.81 m s^{-2}), and Δz is the height of the wind speed and air temperature data (2 m).

The latent heat flux over sea ice (W m^{-2}) is given as (*e.g.*, EC93),

$$F_{lat,i} = \rho_a L_v C_{Ti} U_a (q_{sat(Ti,s)} - q_a), \quad (39)$$

where L_v is the latent heat of vaporization (2.501×10^6 J m^{-3}), and $q_{sat(Ti,s)}$ is the saturation specific humidity over ice. This quantity is equal to (*e.g.*, WHOI, 2010),

$$q_{sat(Ti,s)} = \frac{0.622 e_{sat,i}}{P_s - 0.378 e_{sat,i}}, \quad (40)$$

where $e_{sat,i}$ is the saturation vapor pressure directly over the ice (Pa), which is equivalent to (*e.g.*, WHOI, 2010),

$$e_{sat,i} = 10^{\frac{0.7859 + 0.03477 T_{i,s}}{1 + 0.00412 T_{i,s}} + 0.00422 T_{i,s} + 2}. \quad (41)$$

As per EC93, the formulas for the sensible and latent heat fluxes over leads and open water (W m^{-2}), $F_{sens,w}$ and $F_{lat,w}$, respectively, are similar to those for ice (Eqs. 32 and 39). For the sensible heat flux over water, the quantity $T_{i,s}$ in Eq. (32) is replaced with T_w to represent the surface water temperature. In Eq. (32), the bulk heat and moisture transfer coefficient over water, C_{Tw}, is determined using Equation 37 with $C_{T0} = 1.0 \times 10^{-3}$ over water, and the bulk Richardson number over water, Ri_{water}, is calculated by replacing T_a with T_w in Eq. (38). The latent heat flux over water is computed by replacing C_{Ti} with C_{Tw} in Equation 39, and $q_{sat(Ti,s)}$ with $q_{sat(Tw)}$, the saturation specific

humidity over water. The quantity is computed from Equation 40, however saturation vapor pressure directly over water, $e_{sat,w}$ (Pa), is determined by replacing $T_{i,s}$ with T_w in Equation 41, and multiplying Eq. (41) by 0.98.

The downward longwave (infrared) radiative flux from the atmosphere to the ocean and ice (Wm^{-2}) is defined by (*e.g.*, Konig-Langlo and Augstein, 1994),

$$F_{LW} = (0.765 + 0.22T_{cc}^3)\sigma T_a^4, \quad (42)$$

where the quantity $(0.765 + 0.22T_{cc}^3)$ represents the atmospheric emissivity as a function of the total fractional cloud cover area.

2.2.6 Albedo

The surface albedo parameterization follows the scheme used in EC93, in which there are five surface types considered: dry snow, melting snow, bare ice, meltwater ponds, and open water. The albedo scheme additionally considers the spectral variation in the incoming shortwave radiation in four ranges of wavelength, as well as the albedo dependence on solar zenith angle. The solar zenith angle is given by,

$$\theta_0 = \text{acos}(\mu_0), \quad (43)$$

where the quantity μ_0 is defined as,

$$\mu_0 = \sin(\phi)\sin(\delta) + \cos(\phi)\cos(\delta)\cos(\theta_h). \quad (44)$$

In Eq. (44), δ is defined as (*e.g.*, NOAA, 2015),

$$\delta = 0.006918 - 0.399912\cos(d) + 0.070257\sin(d) - 0.006758\cos(2d) + 0.000907\sin(2d) - 0.002697\cos(3d) + 0.00148\sin(3d), \quad (45)$$

where the quantity d is defined by $d = \frac{2\pi(J-1)}{365.2422}$ and is given in radians. In Eq. (44), θ_h is the hour angle, and is defined as $\theta_h = 15(T_{hr} - M) - L_m$, in which T_{hr} is the hour of the day (*e.g.*, 13 for 13:00) and M is defined by (*e.g.*, NCEP, 2015),

$$M = 12 + 0.12357\sin(d) - 0.004289\cos(d) + 0.153809\sin(2d) + 0.060783\cos(2d). \quad (46)$$

The relative weights assigned to each wavelength band of the solar spectrum, as well as the fractions of diffuse versus direct radiation, are summarized in Table 2 as a function of month (*e.g.*, EC93).

Table 2. Summary of solar spectrum relative weights as a function of wavelength band and month, as well as fractions of diffuse versus direct radiation (EC93).

Solar Spectrum Weights and Radiation Fractions for Surface Albedo						
Month	**Wavelength Band (μm)**				**Diff. Rad. (DR) Fraction**	**Direct Rad. (1 – DR) Fraction**
	0.25 - 0.69	**0.69 - 1.19**	**1.19 - 2.38**	**2.38 - 4.00**		
Jan	0.520	0.343	0.129	0.008	0.779	0.221

Feb	0.520	0.343	0.129	0.008	0.779	0.221
Mar	0.503	0.343	0.142	0.012	0.658	0.342
Apr	0.492	0.339	0.153	0.016	0.489	0.511
May	0.504	0.338	0.144	0.014	0.581	0.419
Jun	0.527	0.340	0.124	0.009	0.724	0.276
Jul	0.545	0.315	0.130	0.010	0.698	0.302
Aug	0.539	0.321	0.130	0.010	0.715	0.285
Sep	0.517	0.339	0.134	0.010	0.717	0.283
Oct	0.519	0.343	0.130	0.008	0.790	0.210
Nov	0.520	0.343	0.129	0.008	0.779	0.221
Dec	0.520	0.343	0.129	0.008	0.779	0.221

The albedo is then given as (*e.g.*, EC93),

$$\alpha = (DR)\left(\Sigma_{j=1}^{4} w_j \alpha_{j(DR)}\right) + (1 - DR)\left(\Sigma_{j=1}^{4} w_j \alpha_{j(1-DR)}\right), \quad (47)$$

where w_j is the weight of a given wavelength band, α_j is the albedo in that band, DR refers to the fraction of diffuse radiation, and $(1 - DR)$ refers to the fraction of direct radiation. Table 3 summarizes the albedo values as functions of the wavelength band of the incoming shortwave radiation spectrum, the surface type, direct or diffuse radiation, and ice and snow thickness, and is reproduced here from Table 2 in EC93.

Table 3. Spectral albedos for the various surface types, reproduced here from Table 2 in EC93.

Spectral Albedos for Five Surface Types				
Surface Type	**Wavelength Band (μm)**			
	0.25 - 0.69	**0.69 - 1.19**	**1.19 - 2.38**	**2.38 - 4.00**
Dry snow, α_s				
Direct Rad.	0.980 - 0.008μ_0	0.902 - 0.116μ_0	0.384 - 0.222μ_0	0.053 - 0.047μ_0
Diffuse Rad.	0.975	0.832	0.250	0.025
Melting snow, α_s				
$h_s \geq$ 0.1m	0.871	0.702	0.079	0.010
$h_s <$ 0.1m	linearly reduced to bare sea ice value	linearly reduced to bare sea ice value	linearly reduced to bare sea ice value	linearly reduced to bare sea ice

				value
Bare sea ice, α_i				
h_i < 1m	0.760 + 0.140ln(h_i)	0.247 + 0.029ln(h_i)	0.055	0.036
1m ≤ h_i <2m	0.770 + 0.018(h_i - 1)	0.247 + 0.196(h_i - 1)	0.055	0.036
h_i ≥ 2m	0.778	0.443	0.055	0.036
Meltwater pond, α_p	0.150 + exp(-8.1h_p - 0.47)	0.054 + exp(-31.8h_p - 0.94)	0.033 + exp(-2.6h_p - 3.82)	0.030
Open water/leads, α_w				
Direct Rad.	α_w* + 0.008	α_w* - 0.007	α_w* - 0.007	α_w* - 0.007
Diffuse Rad.	0.060	0.060	0.060	0.060

In Table 3, h_s is snow depth (m), and the value α_w^* is defined as (*e.g.*, EC93),

$$\alpha_w^* = \frac{0.026}{\mu_0^{1.7}+0.065} + 0.015(\mu_0 - 0.1)(\mu_0 - 0.5)(\mu_0 - 1.0). \quad (48)$$

2.2.7 Energy balance and thickness changes over snow and ice

The energy balance at the surface of the snow or snow-free ice layer is represented by (*e.g.*, EC93),

$$(F_{net})_0 = \epsilon(F_{LW} - \sigma T_0^4) + (1 - \alpha)(1 - I_0)F_{SW} - F_{sens} - F_{lat} = -(F_c)_0, \quad (49)$$

where ϵ is the emissivity of the snow or ice (0.99), T_0 is the temperature of the snow or ice surface (K), α is the snow or ice albedo, and $(F_c)_0$ is the conductive heat flux at the snow or ice surface (W m^{-2}). Eq. (49) is used to solve for the snow or snow-free ice surface temperature after the first time-step.

Changes in snow and ice thickness are governed by the energy balances at the snow and ice surfaces and the base of the ice, and the volumetric heats of fusion for snow and ice. The rate of change in snow thickness at the surface is given by (*e.g.*, EC93),

$$\left(\frac{\partial h_s}{\partial t}\right)_0 = \frac{-F_{net}-(F_c)_0}{L_{fs}}, \quad (50)$$

where L_{fs} is the volumetric heat of fusion for snow (1.097×10^8 J m^{-3}). Similarly, the rate of change in thickness at the surface of the snow-free ice is given by (*e.g.*, EC93),

$$\left(\frac{\partial h_i}{\partial t}\right)_0 = \frac{-F_{net}-(F_c)_0}{L_{fi}}, \quad (51)$$

where L_{fi} is the volumetric heat of fusion for ice (3.014×10^8 J m^{-3}). Changes in thickness at the ice surface are constrained to be $\left(\frac{\partial h_i}{\partial t}\right)_0 \leq 0$ so that ice growth only occurs through accretion at the base. The accretion or melting at the base of the ice is defined by (*e.g.*, EC93),

$$\left(\frac{\partial h_i}{\partial t}\right)_b = \frac{(F_c)_b - F_b}{L_{fb}}, \quad (52)$$

where $(F_c)_b$ is the conductive heat flux at the base of the ice (W m^{-2}), and L_{fb} is the volumetric heat of fusion for ice at the base (2.679×10^8 J m^{-3}).

2.3 Dynamic model description

The dynamic model is based on the Smoothed Particle Hydrodynamics (SPH) formulation as originally applied to ice dynamics in Gutfraind and Savage, 1997 and Lindsay and Stern, 2004. The dynamic model is coupled to the thermodynamic model, and is run at each time-step immediately after the thermodynamic model. It is forced by surface wind speed and direction, surface current speed and direction, Coriolis deflection, the horizontal gradient of the sea surface slope, internal ice stresses, and a coastal boundary force. As per Lindsay and Stern, 2004, particles which drift within 0.4 of the initial grid spacing are combined into a single particle.

2.3.1 Air drag

The zonal and meridional components of the acceleration (m s^{-2}) on each Lagrangian ice particle due to wind forcing are given by,

$$\overrightarrow{A_{wx}} = \left(\frac{1}{\rho_i h_i}\right)\rho_a C_a \sqrt{(\overrightarrow{u_a} - \overrightarrow{u_i})^2 + (\overrightarrow{v_a} - \overrightarrow{v_i})^2}\,(\overrightarrow{u_a} - \overrightarrow{u_i}),$$

$$\overrightarrow{A_{wy}} = \left(\frac{1}{\rho_i h_i}\right)\rho_a C_a \sqrt{(\overrightarrow{u_a} - \overrightarrow{u_i})^2 + (\overrightarrow{v_a} - \overrightarrow{v_i})^2}\,(\overrightarrow{v_a} - \overrightarrow{v_i}), \quad (53)$$

respectively, where C_a is the dimensionless air drag coefficient (2.0×10^{-3}), $\overrightarrow{u_a}$ and $\overrightarrow{u_i}$ are the zonal velocities for wind and ice drift, respectively, and $\overrightarrow{v_a}$ and $\overrightarrow{v_i}$ are the meridional velocities for wind and ice drift, respectively (m s^{-1}).

2.3.2 Water drag

The zonal and meridional components of the acceleration (m s^{-2}) on the ice particles due to ocean current forcing are similar to those for the wind and are given by,

$$\overrightarrow{A_{ox}} = \left(\frac{1}{\rho_i h_i}\right)\rho_{wo} C_w \sqrt{(\overrightarrow{u_w} - \overrightarrow{u_i})^2 + (\overrightarrow{v_w} - \overrightarrow{v_i})^2}\,(\overrightarrow{u_w} - \overrightarrow{u_i}),$$

$$\overrightarrow{A_{oy}} = \left(\frac{1}{\rho_i h_i}\right)\rho_{wo} C_w \sqrt{(\overrightarrow{u_w} - \overrightarrow{u_i})^2 + (\overrightarrow{v_w} - \overrightarrow{v_i})^2}\,(\overrightarrow{v_w} - \overrightarrow{v_i}), \quad (54)$$

respectively, where ρ_{wo} is the density of seawater (kg m^{-3}), C_w is the dimensionless water drag coefficient (5.0×10^{-3}), and $\overrightarrow{u_w}$ and $\overrightarrow{v_w}$ are the zonal and meridional velocities for the surface current, respectively (m s^{-1}). The density of seawater is computed by (*e.g.*, Fofonoff and Millard Jr., 1983),

$$\rho_{wo} = 999.842594 + 6.793952\times10^{-2}T_w - 9.09529\times10^{-3}T_w^2 + 1.001685\times10^{-4}T_w^3 - 1.120083\times10^{-6}T_w^4 + 6.536332\times10^{-9}T_w^5 + (8.24493\times10^{-1} - 4.0899\times10^{-3}T_w + 7.6438\times10^{-5}T_w^2 - 8.2467\times$$

$10^{-7}T_w^3 + 5.3875 \times 10^{-9}T_w^4)S + (-5.72466 \times 10^{-3} + 1.0227 \times 10^{-4}T_w - 1.6546 \times 10^{-6}T_w^2)S^{1.5} + 4.8314 \times 10^{-4}S^2$, (55)

where T_w is the SST (°C).

2.3.3 Coriolis deflection

The zonal and meridional components of the acceleration (m s^{-2}) on the ice particles due to Coriolis forcing are given by,

$$\overrightarrow{A_{cx}} = f\overrightarrow{v_i},$$

$$\overrightarrow{A_{cy}} = -f\overrightarrow{u_i}, \quad (56)$$

respectively. In Eq. (56), f is the Coriolis parameter (s^{-1}) and is defined by $2\omega_e \sin(\phi)$, where ω_e is the Earth angular speed (7.292115×10^{-5} rad s^{-1}).

2.3.4. Sea surface gradient forcing

The zonal and meridional components of the horizontal gravitational acceleration (m s^{-2}) on the ice particles due to the sea surface gradient are given by,

$$\overrightarrow{A_{gx}} = -g\nabla\overrightarrow{H_x},$$

$$\overrightarrow{A_{gy}} = -g\nabla\overrightarrow{H_y}, \quad (57)$$

respectively, where $\nabla\overrightarrow{H_x}$ and $\nabla\overrightarrow{H_y}$ are the zonal and meridional gradients of the sea surface.

2.3.5. Internal ice stresses

The first step in calculating the internal ice stresses is to project the ice particle positions from their latitude-longitude grid onto a Cartesian grid in order to facilitate computations of distance between the particles. The northing-easting grid chosen for this work is the Mercator projection. Conversions of latitude and longitude to Mercator northing, y, and easting, x, coordinates (m) are defined by,

$$y = R_e k ln\left(\tan\left(\frac{\pi}{4} + \frac{\phi}{2}\right)\right),$$

$$x = R_e k L, \quad (58)$$

respectively, where R_e is the radius of the earth (6371×10^3 m), k is the scale factor for 55°N latitude (1.75), and L is the longitude (radians).

The zonal and meridional components of the acceleration (m s^{-2}) on the ice particles due to internal stress gradients are given by (*e.g.*, Lindsay and Stern, 2004),

$$\overrightarrow{A_{sx}} = \left(\frac{1}{\rho_i h_i}\right)\left(\frac{\partial\sigma_{xx}}{\partial x} + \frac{\partial\sigma_{xy}}{\partial y}\right),$$

$$\overrightarrow{A_{sy}} = \left(\frac{1}{\rho_i h_i}\right)\left(\frac{\partial \sigma_{yy}}{\partial y} + \frac{\partial \sigma_{xy}}{\partial x}\right), \quad (59)$$

respectively, where σ is the internal ice stress tensor (kg s^{-2}). The components of the stress gradients $\frac{\partial \sigma_{xx}}{\partial x}$, $\frac{\partial \sigma_{yy}}{\partial y}$, $\frac{\partial \sigma_{xy}}{\partial x}$, and $\frac{\partial \sigma_{xy}}{\partial y}$ are computed by first calculating the components of the stress tensor at the ice particle positions and then linearly interpolating these values to four points surrounding each ice particle (Figure 6).

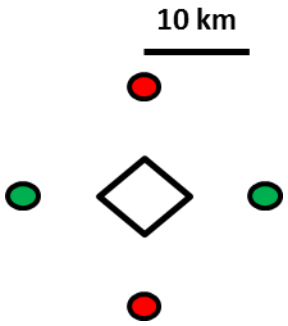

Figure 6. Schematic of the locations at which the ice stress tensor components are computed for calculation of the stress gradients. The white diamond represents an ice particle, the green circles represent the locations between which the zonal stress gradients are computed, and the red circles represent the locations between which the meridional stress gradients are computed. The stress gradient length scale is 10 km (image is slightly altered from original version in Lindsay and Stern, 2004).

In Figure 6, an ice particle is represented by the white diamond. The zonal components of the stress gradients, $\frac{\partial \sigma_{xx}}{\partial x}$ and $\frac{\partial \sigma_{xy}}{\partial x}$, are computed by finite differencing of the stress tensor values at the green circles, and the meridional components of the stress gradients, $\frac{\partial \sigma_{yy}}{\partial y}$ and $\frac{\partial \sigma_{xy}}{\partial y}$, are computed by finite differencing of the stress tensor values at the red circles.

The values of the stress tensor (kg m s^{-2}) are calculated as follows for each ice particle (*e.g.*, Gutfraind and Savage, 1997),

$$\sigma_{xx} = P_i - 2\eta\left(\dot{\epsilon}_{xx} - 0.5\left(\dot{\epsilon}_{xx} + \dot{\epsilon}_{yy}\right)\right),$$

$$\sigma_{yy} = \frac{\sigma_{xx}(1-\sin(\phi_i))}{1+\sin(\phi_i)},$$

$$\sigma_{xy} = -2\eta\dot{\epsilon}_{xy}, \quad (60)$$

where P_i is the internal ice pressure (N m^{-2}), η is the ice viscosity (kg m^{-1} s^{-1}), $\dot{\epsilon}_{xx}$, $\dot{\epsilon}_{yy}$, and $\dot{\epsilon}_{xy}$ are the components of the strain rate tensor (s^{-1}), and ϕ_i is the internal ice friction angle (approximately 17.5°). The evaluation of σ_{yy} as a function of the other principal stress component, σ_{xx}, satisfies the Mohr-Coulomb yield criterion for a plastic regime as per Gutfraind and Savage, 1997. In Eq. (60), the pressure is taken as the ice compressive strength as per Hibler III, 1979 and Sayed et al., 2002 and is defined as,

$$P_i = P^* h_i e^{-20(1-A_{ice})}, \quad (61)$$

where P^* is a sea ice strength constant (5.0×10^3 N m^{-2}). The ice viscosity is defined as (*e.g.*, Gutfraind and Savage, 1997),

$$\eta = \min\left(\frac{P_i \sin(\phi_i)}{\dot{\epsilon}_{xx}-\dot{\epsilon}_{yy}}, \eta_{max}\right), \quad (62)$$

where η_{max} is the maximum possible value of the ice viscosity (1.0×10^{11} kg m^{-1} s^{-1}).

The components of the strain rate tensor are evaluated using the SPH formulation. While the strain rates for any given ice particle are theoretically influenced by all other ice particles in the model domain, it is most computationally practical to assume only a limited number of nearest-neighbor ice particles influence the strain rates of a given particle. In this paper, only the nearest three ice particles are considered when calculating strain rates for a given particle. Coastal boundary particles are considered when finding the nearest-neighbor particles, and their influence on the strain rates of nearby ice particles is treated the same as that from other ice particles. However, coastal cells have fixed zero-velocities and are assumed to be constantly circular with a radius of 5 km. They also exert an additional repulsive force on ice particles (see section 2.3.6).

The influence that a given ice particle exerts on another decreases exponentially with distance between particles, and is most commonly represented through the Gaussian kernel. The two-dimensional Gaussian kernel is defined as (*e.g.*, Gutfraind and Savage, 1997),

$$W(\boldsymbol{r}, L) = \frac{1}{\pi L^2} e^{-\frac{r^2}{L^2}}, \quad (63)$$

where $\boldsymbol{r}$ is the distance from the ice particle for which the strain rates are being calculated to a nearest-neighbor particle (m), and L is a smoothing length (150 km as per Lindsay and Stern, 2004). The components of the strain rate tensor are then given as (*e.g.*, Gutfraind and Savage, 1997),

$$\dot{\epsilon}_{xx} = \Sigma_k \left(-\frac{2I_{area_k}(u_k-u_i)W(\boldsymbol{r},L)_k r_{x_k}}{L^2}\right),$$

$$\dot{\epsilon}_{yy} = \Sigma_k \left(-\frac{2I_{area_k}(v_k-v_i)W(\boldsymbol{r},L)_k r_{y_k}}{L^2}\right),$$

$$\dot{\epsilon}_{xy} = \Sigma_k \left(\frac{-I_{area_k}(v_k-v_i)W(\boldsymbol{r},L)_k r_{y_k} - I_{area_k}(u_k-u_i)W(\boldsymbol{r},L)_k r_{x_k}}{L^2}\right), \quad (64)$$

where I_{area_k} is the total surface are of the k^{th} nearest-neighbor ice particle (m^2), u_k and v_k are the zonal and meridional velocities of the k^{th} nearest-neighbor ice particles, respectively (m s^{-1}), u_i and v_i are the zonal and meridional velocities of the ice particle for which the strain rate tensor is being calculated, respectively (m s^{-1}), and r_{x_k} and r_{y_k} are the zonal and meridional distances from the ice particle for which the strain rates are being calculated to the k^{th} nearest-neighbor particle (m). The surface areas of the ice particles are calculated at each time-step using Voronoi tessellation over the whole model domain as per Lindsay and Stern, 2004. For each ice particle, the Voronoi polygon covers the area surrounding the particle which is closer to that particle than to any other.

2.3.6 Coastal boundary force

In order to prevent ice particles from drifting past the coastal boundary cells, a repulsive force from each coastal cell is exerted on every ice particle in the direction of the vector pointing from the coastal cell toward the ice particle. As per Lindsay and Stern, 2004, the force is given in the form $\frac{1}{\boldsymbol{R}^2}$, where $\boldsymbol{R}$ is the distance from the coastal cell to the ice particle. The force is set to be 0.1 N m^{-2} at a distance of 25 km. An identical repulsion force is also exerted on ice particles from the boundaries of the model domain in the ocean in order to keep ice particles from drifting outside the model domain.

2.3.7 Dynamic evolution of ice thickness and concentration

Changes in the ice thickness and concentration of particles due to dynamics are determined by the principal components of the strain rate tensor as follows,

$$\frac{\partial h_i}{\partial t} = -h_i\left(\dot{\epsilon}_{xx} + \dot{\epsilon}_{yy}\right),$$

$$\frac{\partial A_{ice}}{\partial t} = -A_{ice}\left(\dot{\epsilon}_{xx} + \dot{\epsilon}_{yy}\right), \tag{65}$$

respectively. The dynamically induced changes in ice thickness and concentration are then added to any thermodynamically induced changes in these parameters at each time-step.

2.4 Time-stepping schemes

Several numerical integration schemes for time-stepping are used in the present model. The Euler-forward scheme (*e.g.*, Khandekar, 1980) is used to solve the thermodynamic equations for changes in snow and ice thickness (Eqs. 50-52), changes in snow and ice temperature due to solar radiation penetration (Eqs. 18, 20-21), and snow accumulation. This scheme is used to calculate changes from the first to second time-step in melt-pond depth (Eq. 22), water temperature beneath the base of the ice (Eq. 29), and lead area fraction (Eq. 27). The Euler-forward scheme is additionally used in the dynamic model to integrate the ice particle velocities to position displacements, to update the dynamically forced changes in ice thicknesses and concentrations (Eq. 65), and to integrate the initial ice accelerations to velocities from the first time-step to the second. The Euler-forward scheme is represented by,

$$X_{i+1} = X_i + \Delta t \left(\frac{\partial F}{\partial t}_i\right) : i = 1, \tag{66}$$

where X is the variable being solved, i is the time-step index, Δt is the time-step (seconds), and F is the function of X differentiated with respect to time, t.

The second-order Adams-Bashforth scheme (*e.g.*, Khandekar, 1980) is used to solve thermodynamic equations for changes in melt-pond depth (Eq. 22), water temperature beneath the base of the ice (Eq. 29), and lead area fraction (Eq. 27) from the second to the fourth time-steps. This scheme is also used to solve the changes in ice particle velocities from the second to the fourth time-steps in the dynamic model. The second-order Adams-Bashforth scheme is represented by,

$$X_{i+1} = X_i + \Delta t\left(1.5\frac{\partial F}{\partial t_i} - 0.5\frac{\partial F}{\partial t_{i-1}}\right): 1 < i \leq 3. \quad (67)$$

The fourth-order Adams-Bashforth scheme (*e.g.*, Matthews and Fink, 2004) is used to solve for changes in melt-pond depth (Eq. 22), water temperature beneath the base of the ice (Eq. 29), and lead area fraction (Eq. 27) from the fourth time-step onward in the thermodynamic model. In the dynamic model, the fourth-order Adams-Bashforth predictor-corrector scheme (*e.g.*, Matthews and Fink, 2004) is used to solve the ice velocity changes from the fourth time-step onward. The fourth-order Adams-Bashforth predictor-corrector scheme is represented by,

$$X_{i+1} = X_i + \frac{\Delta t}{24}\left(55\frac{\partial F}{\partial t_i} - 59\frac{\partial F}{\partial t_{i-1}} + 37\frac{\partial F}{\partial t_{i-2}} - 9\frac{\partial F}{\partial t_{i-3}}\right),$$

$$X_{i+1} = X_i + \frac{\Delta t}{24}\left(9\frac{\partial F}{\partial t_{i+1}} + 19\frac{\partial F}{\partial t_i} - 5\frac{\partial F}{\partial t_{i-1}} + \frac{\partial F}{\partial t_{i-2}}\right): i > 3, \quad (68)$$

where the first line represents the fourth-order Adams-Bashforth scheme, and both lines represent the sequential steps of the combined predictor-corrector scheme.

The one-dimensional heat equations for the snow and ice temperatures (Eqs. 1 and 7) in the thermodynamic model are solved using the standard Euler-forward scheme and centred finite-differencing for second-order differential equations between the first and second time-steps, and the Dufort-Frankel algorithm (*e.g.*, EC93 and Mitchell and Griffiths, 1980) from the second time-step onward. The Euler-forward scheme with centred finite-differencing is represented by (*e.g.*, MacKinnon, 2015),

$$X_{i+1}^j = X_i^j + \frac{\kappa\Delta t}{\Delta z^2}\left(X_i^{j+1} - 2X_i^j + X_i^{j-1}\right): i = 1, \quad (69)$$

where j is the depth level index in the snow or ice layer, κ is the quotient of the thermal conductivity and the volumetric heat capacity for snow or ice, and Δz is the spacing between depth levels (m). The Dufort-Frankel algorithm is represented by (*e.g.*, MacKinnon, 2015),

$$X_{i+1}^j = \left(\frac{1-\beta}{1+\beta}\right)X_{i-1}^j + \left(\frac{\beta}{1+\beta}\right)\left(X_i^{j+1} + X_i^{j-1}\right), \quad (70)$$

where β represents the quantity $2\frac{\kappa\Delta t}{\Delta z^2}$.

Acceptable numerical stability of the integration schemes is achieved when a time-step Δt of one hour (3600 seconds) is used for the thermodynamic model-only runs, and a time-step of one minute (60 seconds) is used for the thermodynamic-dynamic coupled model runs.

2.5 Model input

The atmospheric inputs to the model include the 2 m air and dew-point temperatures, relative humidity, 10 m wind speed and direction, surface pressure, total cloud cover area fraction, snowfall, and total precipitation. All atmospheric parameters except for precipitation are taken from the North American Regional Reanalysis (NARR), which has an approximately 0.3° spatial resolution (about 33.3 km) and a three-hourly temporal resolution. In order

to make the wind speed more realistic for near surface winds, a logarithmic wind profile law is used to scale the 10 m height wind speeds to 2 m (*e.g.*, ISO 19901-1),

$$U_a = U_{a_{10m}}\left(1 + 0.0573\sqrt{1 + 0.15U_{a_{10m}}}\right)\ln\left(\frac{2}{10}\right), \quad (71)$$

where $U_{a_{10m}}$ is the NARR wind speed at 10 m (m s^{-1}).

The snowfall and total precipitation data are given in meters of water equivalent over the dataset time-step and are taken from the European Centre for Medium-Range Weather Forecasting (ECMWF) ERA-Interim Reanalysis, which has a 0.5°-0.75° spatial resolution (about 55.5-83 km) and a six-hourly temporal resolution. Rainfall is assumed to be the difference of the total precipitation and the snowfall. In order to convert the ECMWF snowfall data from meters of water equivalent to actual snow accumulation, SF, the following relationship to 2 m air temperature is used (*e.g.*, NWS, 1996),

$$SF = 5SF_w, T_a \geq 0,$$

$$SF = 10SF_w, 0 > T_a \geq -1.1,$$

$$SF = 15SF_w, -1.1 > T_a \geq -3.9,$$

$$SF = 20SF_w, -3.9 > T_a \geq -7.8,$$

$$SF = 30SF_w, -7.8 > T_a \geq -11.1,$$

$$SF = 40SF_w, -11.1 > T_a \geq -15,$$

$$SF = 50SF_w, T_a < -15, \quad (72)$$

where SF_w is the snowfall rate in meters of water equivalent (m s^{-1}), and T_a is in °C.

The ice and oceanographic inputs to the model include the sea surface temperature, sea surface salinity, surface current speed and direction, sea surface height above the geoid, and sea ice thickness, concentration, and drift speed and direction. The ice and oceanographic parameters are taken from the Operational Mercator global Ocean analysis and forecast system. This dataset has a 0.08° spatial resolution (approximately 8.9 km), a two-hourly temporal resolution for sea surface temperature, sea surface salinity, and surface current speed and direction, and a daily-mean temporal resolution for sea surface height above the geoid, and sea ice thickness, concentration, and drift speed and direction. In this dataset, the sea surface temperature, salinity, currents, and height are initially derived from the Nucleus for European Models of the Ocean (NEMO 3.1), while the sea ice thickness, concentration, and velocity are derived from the LIM2 sea ice model. Sea surface height anomaly data derived from the Jason2, Cryosat, and Saral-Altika satellites are assimilated into the dataset, as well as sea surface temperature data from the Reynolds AVHRR-AMSR ¼° satellite, and in-situ profiles of ocean temperature and salinity. The sea ice thickness, concentration, and velocity are used to initialize the model, while the remaining metocean parameters described above are used to force the model for the duration of a run.

Finally, the Labrador coastal boundaries are included, and well as the ocean bathymetry (*e.g.*, GEBCO, 2008, 30-second data). All dynamic input data are spatially and temporally linearly interpolated as needed.

2.6 Comparison of LIM2 sea ice data with CIS ice charts

Given the fact that the LIM2 sea ice dataset used here to initialize the model and compare model results to the "best estimate" of sea ice conditions is itself derived from a model, it is worth comparing the LIM2 ice data from the current model run period of April-May 2015 for the Labrador coast with observations from the CIS ice charts. The LIM2 dataset was used in this study due to its relatively high temporal (daily) resolution compared to the weekly-mean resolution of the CIS digitized ice charts. Figure 7-Figure 15 show the normalized errors between the weekly average CIS chart and the LIM2 ice concentration and thickness for April-May 2015 for central coastal Labrador from Makkovik north to Nain. Here, the normalized (dimensionless) error is defined as,

$$E_{C,T} = \frac{CIS_{C,T} - LIM2_{C,T}}{CIS_{C,T}}, \tag{73}$$

where $CIS_{C,T}$ is the ice concentration (0-1) or thickness (m) of a given domain grid point from the CIS chart, and $LIM2_{C,T}$ is the ice concentration (0-1) or thickness (m) of the same grid point from the LIM2 dataset.

Figure 7-Figure 15 show that the LIM2 dataset is fairly close to the CIS charts in terms of ice concentration and thickness for this period in the areas of the model domain closer to shore. The LIM2 dataset simulates greater ice concentrations and thicknesses further offshore than the CIS charts show. However, the present paper focuses on simulating ice conditions close to the Labrador coast from near Makkovik up to Nain; hence the LIM2 dataset can be considered reliable for the purposes of this study. Note that the LIM2 model does not simulate the land-fast ice cover directly along the shoreline, whereas the CIS charts show the land-fast ice. However, in this paper, the break-up of the land-fast ice is assumed to occur when the deployed buoys began to drift.

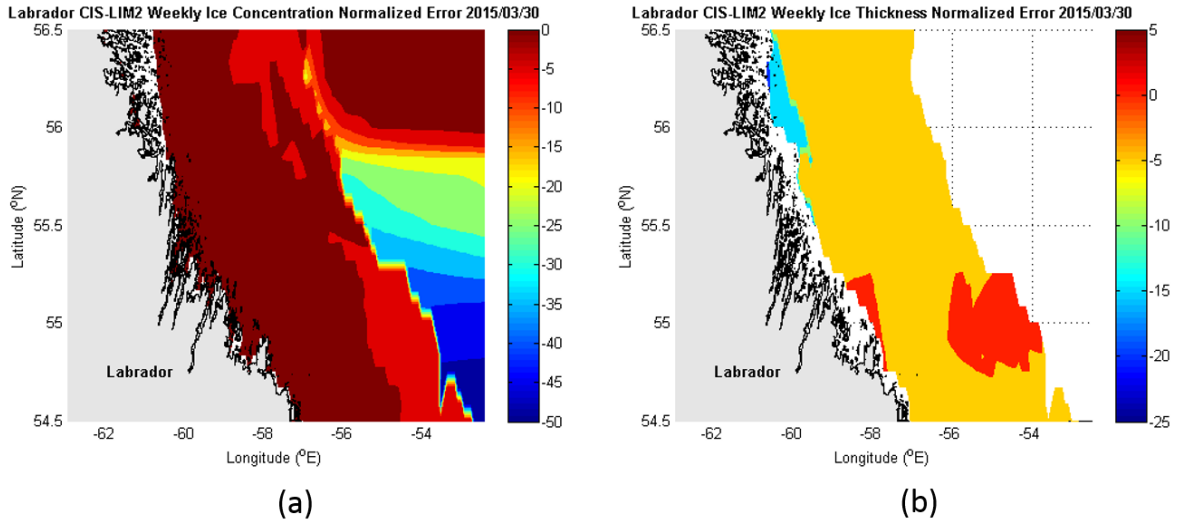

Figure 7. Central coastal Labrador weekly average CIS-LIM2 ice concentration (a) and thickness (b) normalized error for the week of March 30 – April 5, 2015.

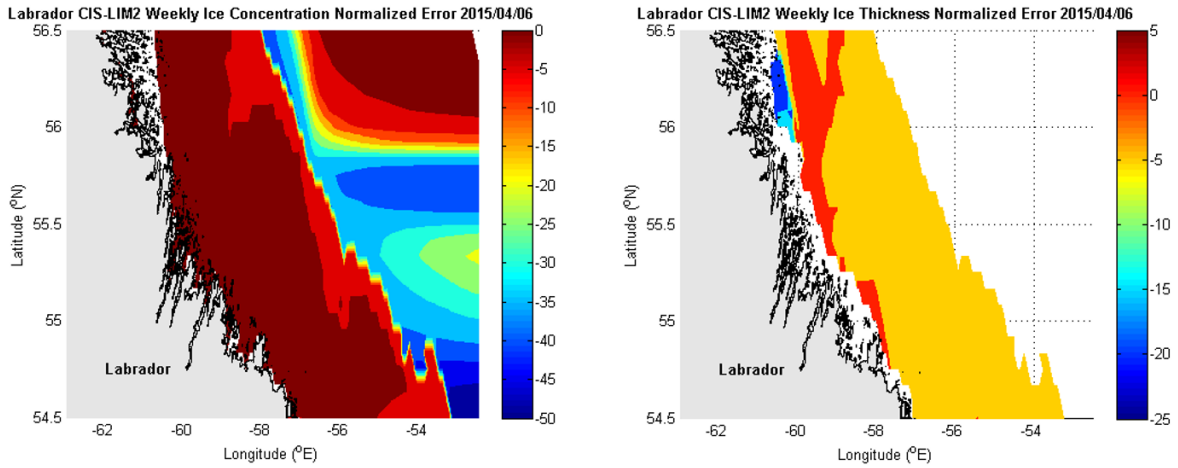

641

642 **Figure 8.** Central coastal Labrador weekly average CIS-LIM2 ice concentration (a) and thickness (b) normalized
643 error for the week of April 6-12, 2015.

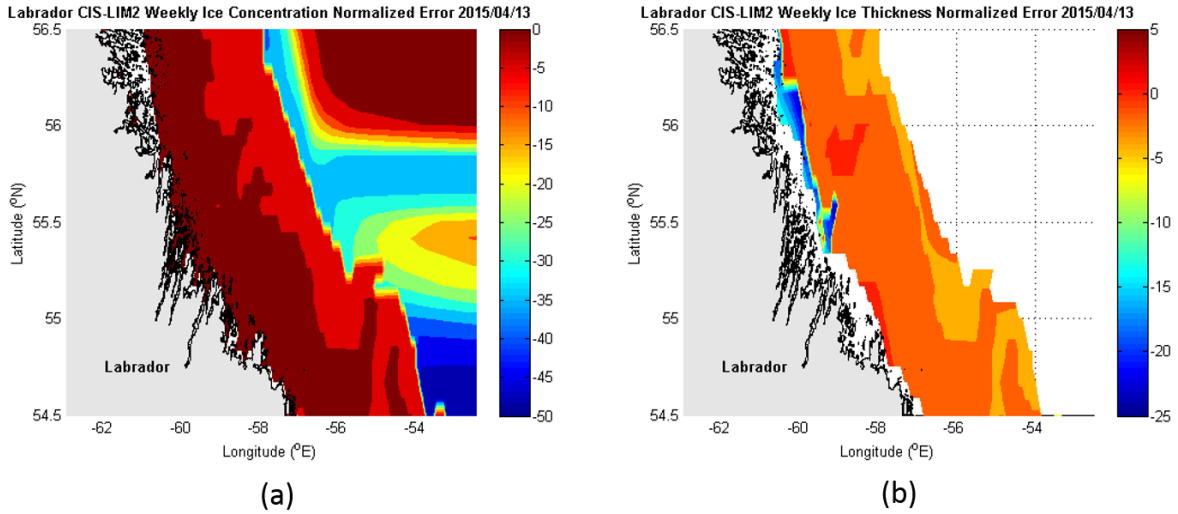

644

645 **Figure 9.** Central coastal Labrador weekly average CIS-LIM2 ice concentration (a) and thickness (b) normalized
646 error for the week of April 13-19, 2015.

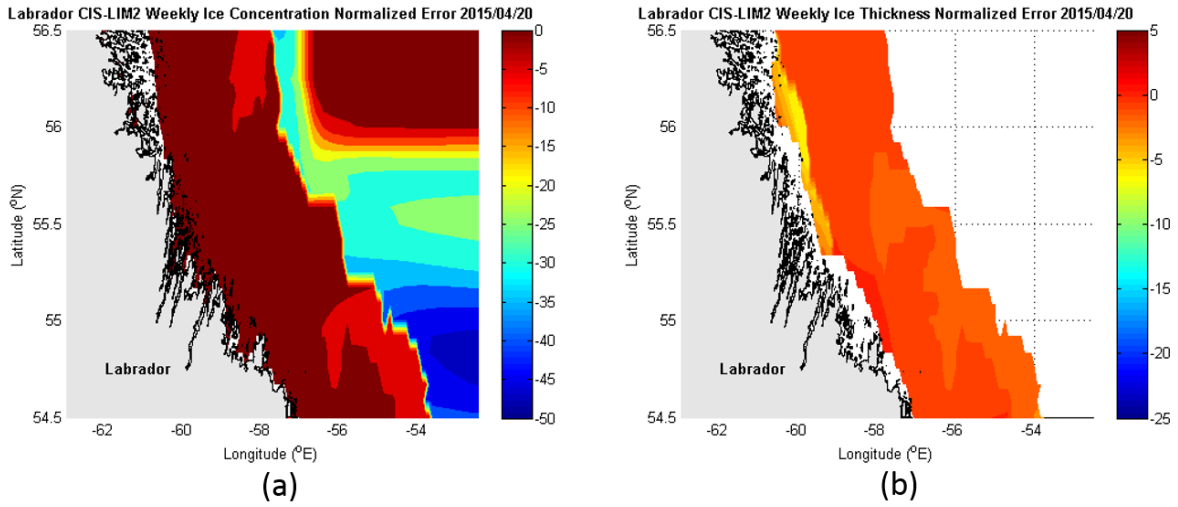

Figure 10. Central coastal Labrador weekly average CIS-LIM2 ice concentration (a) and thickness (b) normalized error for the week of April 20-26, 2015.

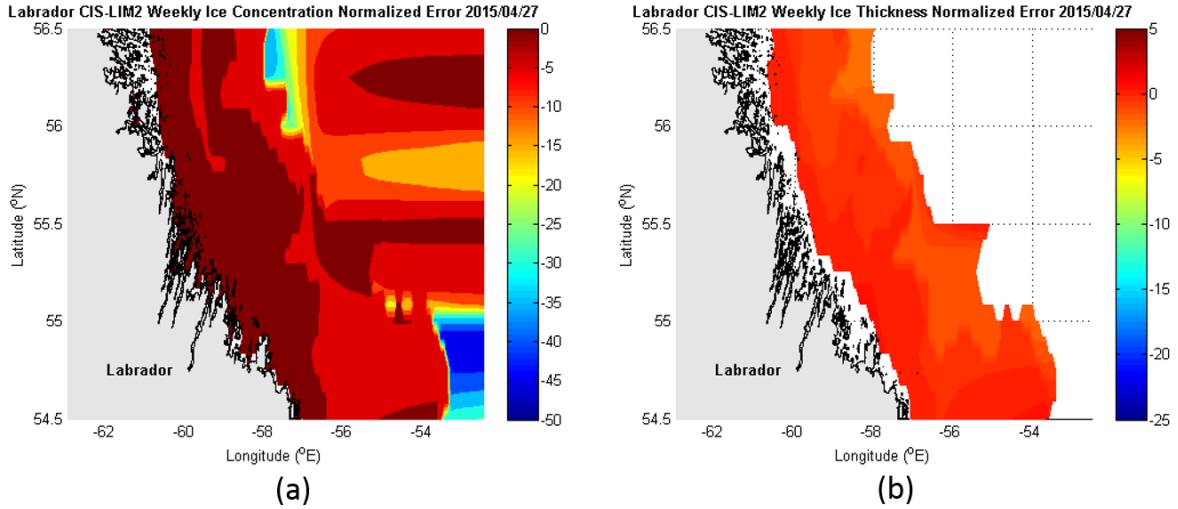

Figure 11. Central coastal Labrador weekly average CIS-LIM2 ice concentration (a) and thickness (b) normalized error for the week of April 27 – May 3, 2015.

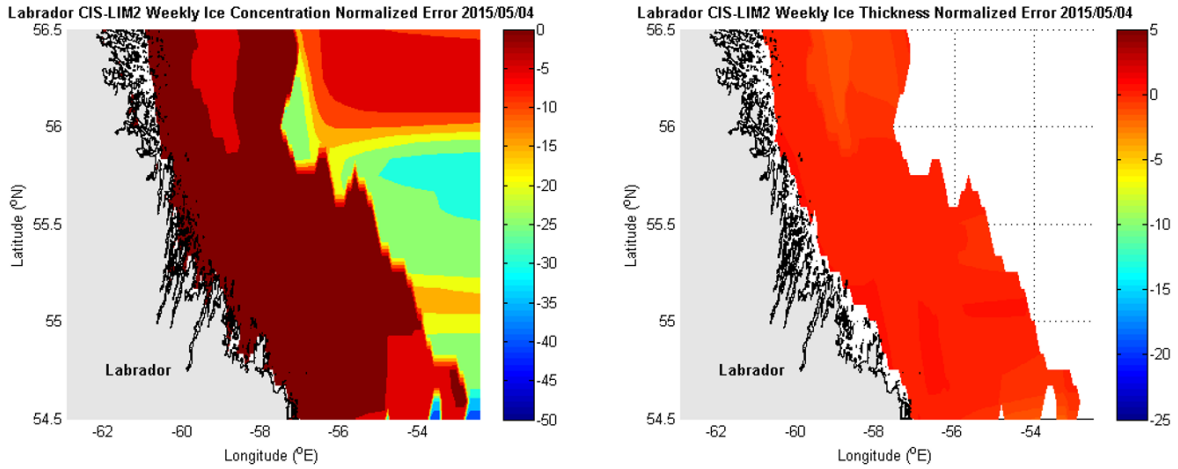

Figure 12. Central coastal Labrador weekly average CIS-LIM2 ice concentration (a) and thickness (b) normalized error for the week of May 4-10, 2015.

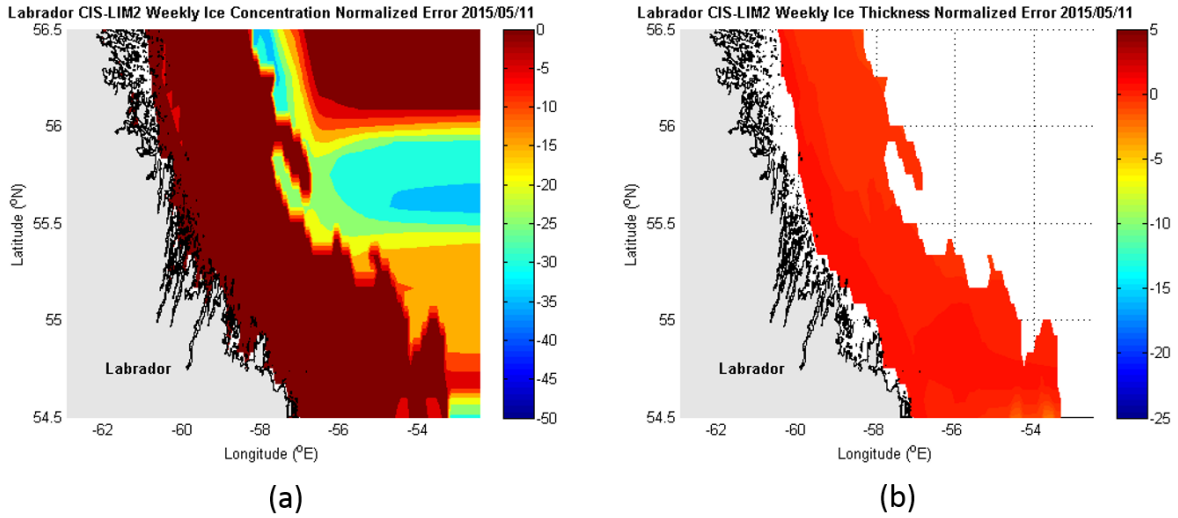

Figure 13. Central coastal Labrador weekly average CIS-LIM2 ice concentration (a) and thickness (b) normalized error for the week of May 11-17, 2015.

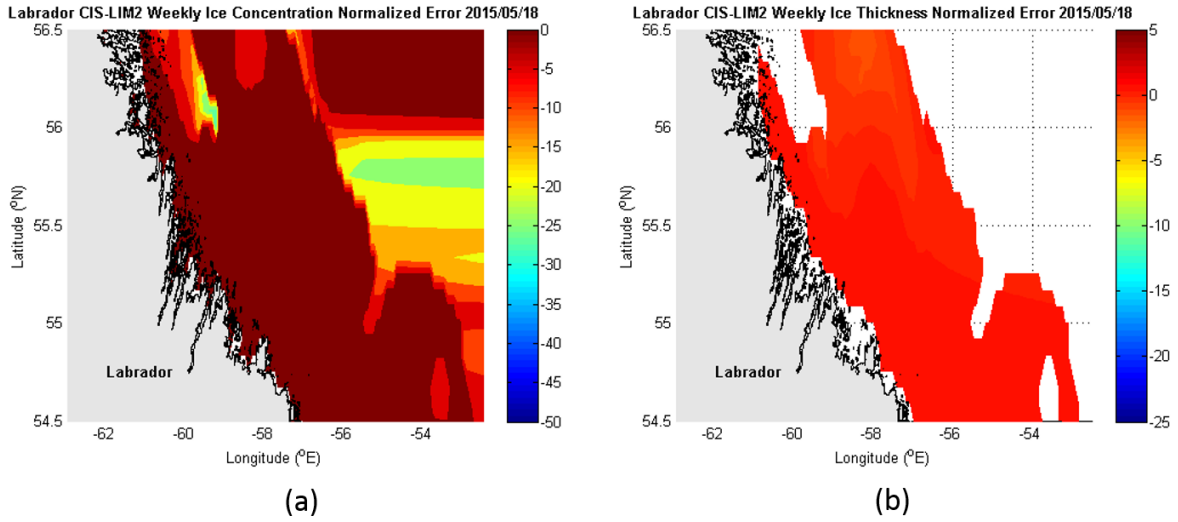

Figure 14. Central coastal Labrador weekly average CIS-LIM2 ice concentration (a) and thickness (b) normalized error for the week of May 18-24, 2015.

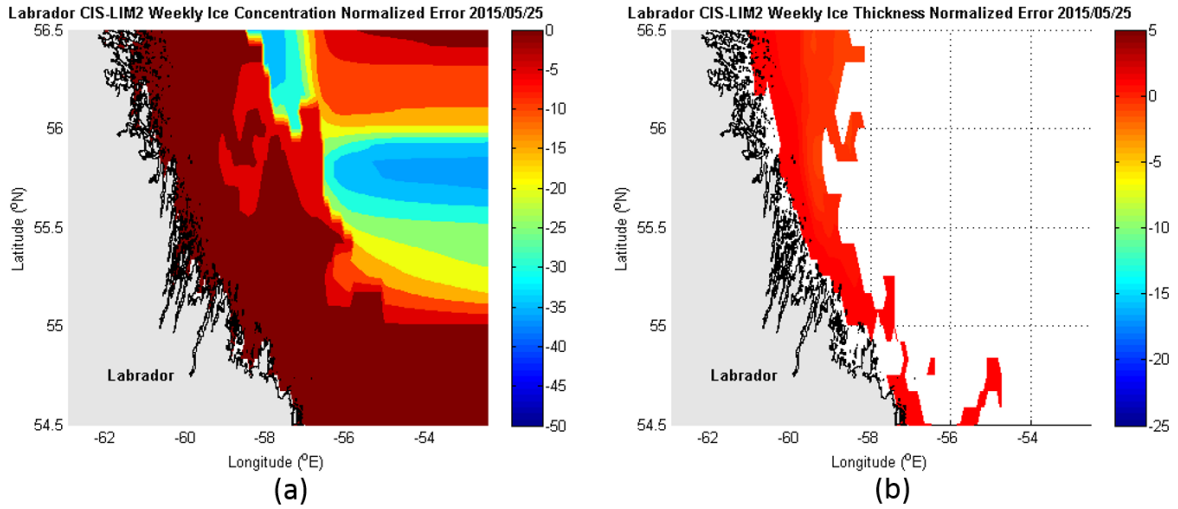

Figure 15. Central coastal Labrador weekly average CIS-LIM2 ice concentration (a) and thickness (b) normalized error for the week of May 25-31, 2015.

3 Model Validation

In this section, results of model runs are presented for the thermodynamic model for April 1 – May 31, 2015, as well as runs of the coupled thermodynamic-dynamic model for May 1-7, 2015. The thermodynamic model run period was selected to cover the observed break-up periods for the land-fast ice offshore Makkovik and Nain. Two of the three ice drift tracking buoys deployed offshore Makkovik began to drift on April 23 (Figure 1), and each of the three buoys deployed offshore Nain began to drift on May 1, 2, and 6, respectively. The shorter thermodynamic-

dynamic model run period was selected to cover most of the observed break-up period for the land-fast ice offshore Nain.

The model runs are initialized with the best estimate of sea ice conditions over the model domain as obtained from the LIM2 sea ice model dataset, and model results here are compared with the LIM2 data. Hereafter, all results from the model presented in this paper are referred to as "model" results, and data from the LIM2 dataset are referred to explicitly. The model domain extends between 62°W and 57.5°W longitude and 55°N and 57°N latitude. For the thermodynamic model-only runs, the parameters of interest which are presented here are the sea ice thickness and concentration. For the thermodynamic-dynamic model, the sea ice thickness, concentration, and velocity are presented. Of particular interest in the present work is the model performance in the regions offshore Makkovik and Nain; hence, additional analyses are given for the temporal evolution of sea ice thickness and concentration in these areas.

The thermodynamic model runs use a 0.45° spatial resolution (approximately 50 km) for initial ice particle spacing and a one-hourly temporal resolution, while the thermodynamic-dynamic model run uses a 0.5° spatial resolution (approximately 55.5 km) for initial ice particle spacing and a one-minute temporal resolution. The higher temporal resolution is needed for the stability of the numerical integration scheme in the dynamic model. Hence, a lower spatial resolution and shorter model run period are used for the dynamic model to lessen the required computation time.

3.1 Thermodynamic model results

The largest uncertainty in the thermodynamic model is the initialization of snow cover on the sea ice. While available reanalysis datasets provide snow depth, they only provide it in meters of water equivalent; however, actual snow depth on the sea ice plays a critical role in the evolution of the ice cover due to the strong insulating effect of snow. Since there do not exist any widespread and frequent snow depth measurements along the Labrador coast, an approximate early spring mean snow depth value of 40 cm is used here to initialize the model on April 1. This depth was taken from measurements of snow depth performed on Lake Melville in March 2009 (*e.g.*, Prinsenberg et al., 2011). It cannot be overstated how uncertain this initial snow depth value is, as it is applied to the entire model domain, and snow depths may be significantly greater further north around Nain. Future use of this model for operational ice forecasting purposes must involve adequate snow depth data acquisition.

In the model results presented here, one model run assumes 40 cm of snow depth over the entire model domain at the start of April 1, 2015, while another model run assumes no snow on the sea ice at the start of the model run on April 1. Both model runs are subject to the same snow accumulation on the ice over the two-month period as forced by the ECMWF snowfall data. Hence, the effect of a significant snow cover on the ice at the start of the melt season can be examined.

Figure 16 shows the initial ice conditions on April 1, 2015 00:00 UTC as given by the LIM2 dataset. The green circle represents the region offshore Makkovik analyzed here, and the purple circle represents the region offshore Nain. There are four model grid points within each of these circled regions over which ice thickness and

concentrations are averaged for the offshore Makkovik and Nain analyses. These two regions were selected to encompass the land-fast ice in the vicinities of Makkovik and Nain so that the timing of the land-fast ice break-up could be modeled and compared with the actual timing of the break-up as recorded by the ice tracking buoys.

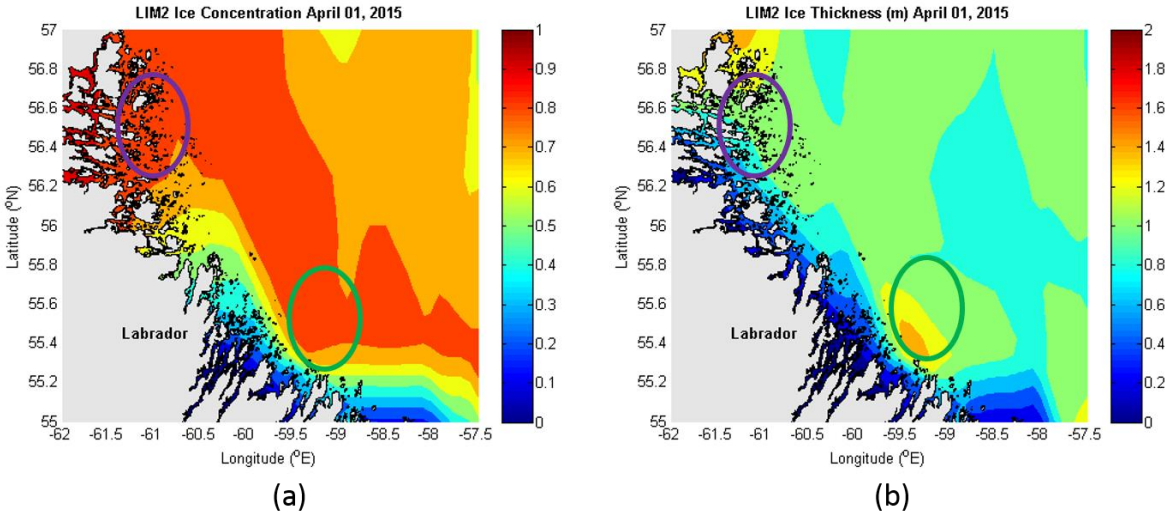

Figure 16. Sea ice concentration (a) and thickness (b) over the model domain at the start of the thermodynamic model runs on April 1, 2015 00:00 UTC, as obtained from the LIM2 dataset. The region circled in green represents the area over which ice conditions offshore Makkovik are analyzed in this section, and the purple circled region represents the area over which ice conditions offshore Nain are analyzed.

Figure 17 shows the evolution of average ice conditions during April 1 – May 31, 2015 in the regions offshore Makkovik (green circles in Figure 16) and Nain (purple circles in Figure 16) according to the LIM2 data, the thermodynamic model with 40 cm of initial snow cover, and the thermodynamic model with no initial snow cover. According to the model run with initial snow cover, the average ice thickness and concentration offshore Makkovik decrease to zero on May 14, while for the run with no initial snow cover, the ice disappears completely around Makkovik on May 1. The progression of the LIM2 ice thickness and concentration near Makkovik shows a somewhat less precipitous decline in ice conditions compared to the model results shown here. While the LIM2 ice thickness and concentration do not reach zero during the model time period, they decline to less than 0.2 m and 0.1, respectively, by May 18 before rebounding slightly as more ice drifts into the region from the north. This minimum in overall average ice conditions offshore Makkovik occurs four days after the model minimum with 0.4 m initial snow cover, and 18 days after the disappearance of ice in the model run with no initial snow cover. In the region offshore Nain, the ice also disappears on May 14 in the model with initial snow cover, and on April 25 in the model without initial snow cover (Figure 17). The LIM2 ice thickness and concentration decrease to zero by May 15.

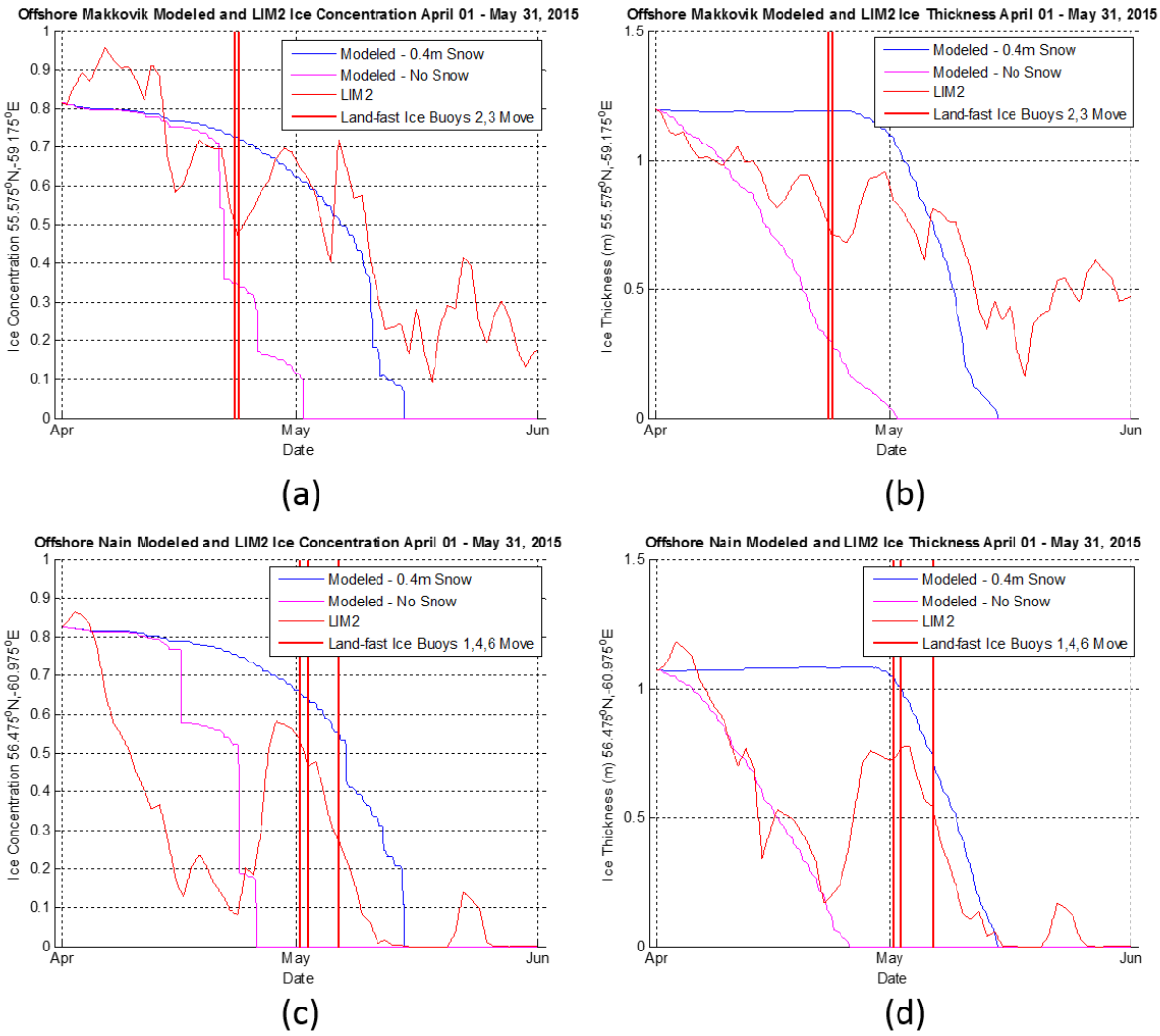

727

728 **Figure 17.** Evolution of average ice concentration (a,c) and thickness (b,d) in the focus regions offshore Makkovik
729 (a,b) and Nain (c,d) during April 1 – May 31, 2015. The thin red lines represent LIM2 ice conditions, the blue lines
730 represent ice conditions for the thermodynamic model presented here initialized with 40 cm of snow, and the
731 magenta lines represent ice conditions for the thermodynamic model initialized with no snow. The thick red lines
732 mark the timing of first recorded movement by the land-fast ice buoys. The latitude-longitude coordinates shown on
733 the y-axes represent the central locations for the regions over which average ice conditions are shown.

734 The thick red lines in Figure 17 mark the times that the land-fast ice buoys first recorded movement, indicating that
735 the break-up of the land-fast ice in those regions had begun. Buoys 2 and 3 began to drift on April 23 around 05:00
736 and 15:00 UTC, respectively, offshore Makkovik, and buoys 1, 4, and 6 began to drift around May 1 10:00, May 2
737 12:00, and May 6 12:00 UTC, respectively, offshore Nain. The model run with 40 cm initial snow cover most
738 accurately predicts the timing of the onset of the land-fast ice break-up with precipitous declines in regional mean
739 ice thickness and concentration commencing immediately after these times. The averaged results for both the
740 Makkovik and Nain regions suggest that there was most likely significant snow cover on the ice on April 1, and that

741 if the model is properly initialized with snow cover conditions, it can reasonably predict the progression and timing
742 of the decline in regional ice concentration and thickness more than a month in advance.

743 At the specific locations at which the ice drift buoys were deployed, Figure 18 shows the modeled ice concentrations
744 and thicknesses near Makkovik and Nain for April 1 – May 31 from the thermodynamic model with 0.4 m of initial
745 snow cover. This model run is not initialized with the LIM2 ice concentration and thickness data, but rather assumes
746 the land-fast ice at these five locations had a concentration and thickness of 0.995 and 0.95 m on April 1,
747 respectively. The assumed ice thickness represents the mean of the normal thickness range for medium first-year ice
748 (0.7-1.2 m), which was the ice type shown for these locations on April 1 on the CIS daily ice charts. In Figure 18,
749 the times at which the modeled ice concentrations first drop below 0.99 and the modeled thicknesses first began to
750 display steep decreases below their original thickness of 0.95 m are used as proxies for the beginning of the local of
751 land-fast ice break-up. These times fall within 4.7 hours to 5.9 days from the times at which the drift buoys began to
752 move at these locations (Table 4).

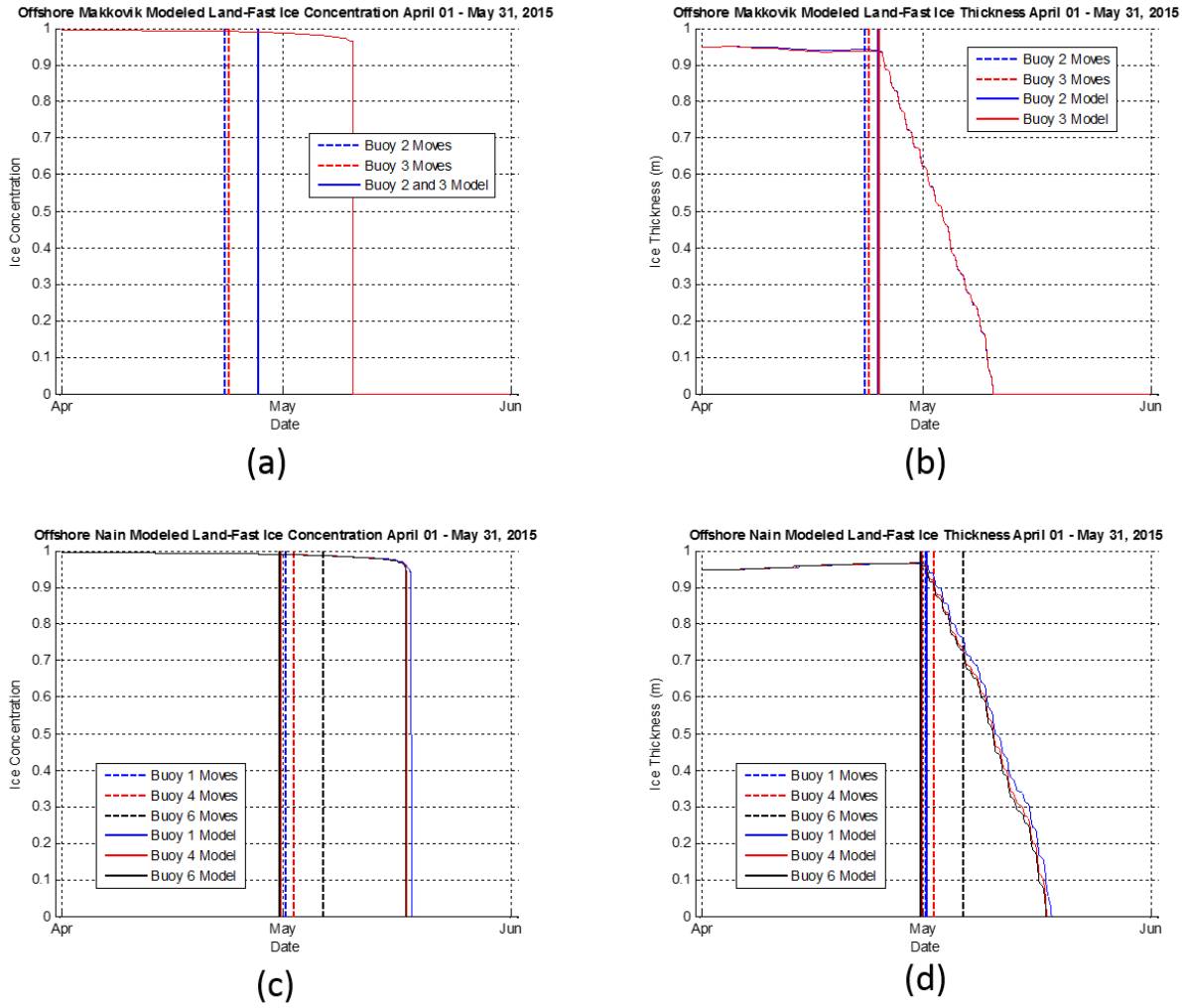

753

754 **Figure 18.** Modeled ice concentration and thickness (thin solid lines) vs. time at the buoy deployment locations near
755 Makkovik (a,b) and Nain (c,d). The vertical dashed lines represent the times at which the buoys first recorded
756 motion, the vertical solid lines represent the times at which the modeled ice concentrations begin to fall below 0.99
757 (a,c), and the times at which the modeled ice thicknesses first fall below 0.95 m (all times in UTC).

758 **Table 4.** Summary of buoy deployment locations, modeled and observed land-fast ice break-up times according to
759 concentration and thickness criteria described above, and observed minus modeled break-up time error ranges.

Buoy	**Deployment Coordinates**	**Modeled Break-Up Time (Thickness)**	**Modeled Break-Up Time (Concentration)**	**Observed Break-Up Time**	**Observed - Modeled Error Range (hours)**
1	56.45°N, 60.78°W	May 01 14:00	April 30 17:00	May 01 09:18	-4.7 to 16.3

2	55.29°N, 59.24°W	April 24 21:00	April 27 14:00	April 23 04:32	-105.5 to -40.5
3	55.28°N, 59.19°W	April 25 02:00	April 27 14:00	April 23 14:14	-95.8 to -35.8
4	56.40°N, 60.80°W	April 30 20:00	April 30 16:00	May 02 11:26	39.4 to 43.4
6	56.39°N, 60.84°W	April 30 18:00	April 30 15:00	May 06 11:38	137.6 to 140.6

Figure 19 shows contour plots of the modeled and LIM2 ice thickness and concentration across the model domain 24 days into the model run, and one day after the first land-fast ice buoys offshore Makkovik began to drift. The model results shown in Figure 19 are from the run initialized with 0.4 m of snow cover. The model shows little change in ice thicknesses by April 24 compared to April 1, with some decrease in ice concentrations. The LIM2 data show a comparatively more extensive retreat in ice thicknesses and concentrations by April 24; however, both the LIM2 data and the model results show a large region of ice concentrations around 0.7 toward the coast, with concentrations around 0.6 immediately to the east.

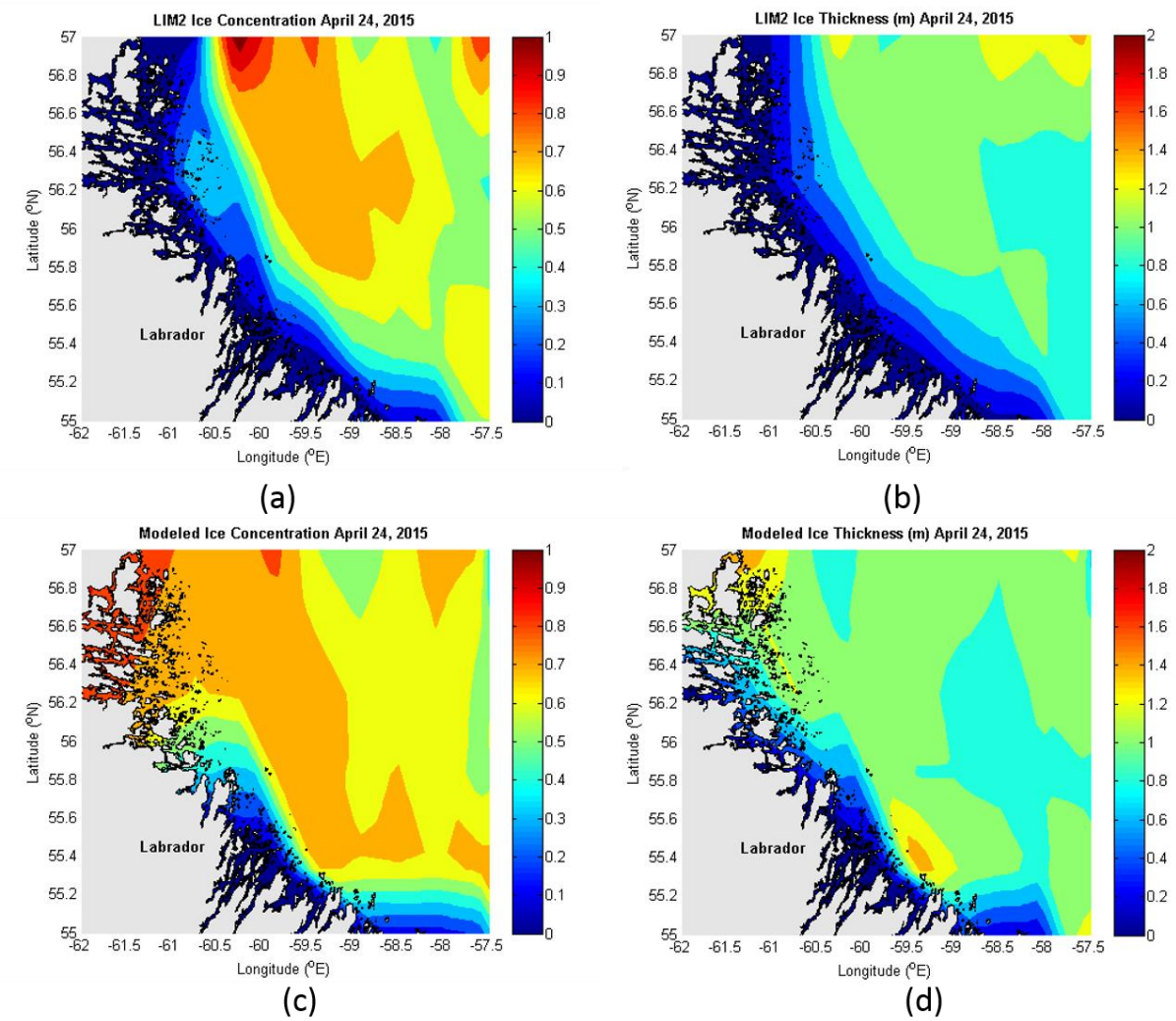

767

768 **Figure 19.** Sea ice concentration (a,c) and thickness (b,d) on April 24, 2015 03:00 UTC (00:00 AST) from LIM2
769 data (a,b) and the thermodynamic model presented here (c,d). The results of the thermodynamic model run shown
770 here are initialized with 40 cm of snow.

771 The results in Figure 20 show that when the thermodynamic model is initialized with no snow cover on April 1,
772 nearly all the ice disappears by April 24. In this model run, the ice disappears completely from the model domain by
773 May 2, which indicates that it is not a realistic scenario to initialize the model without a snow cover.

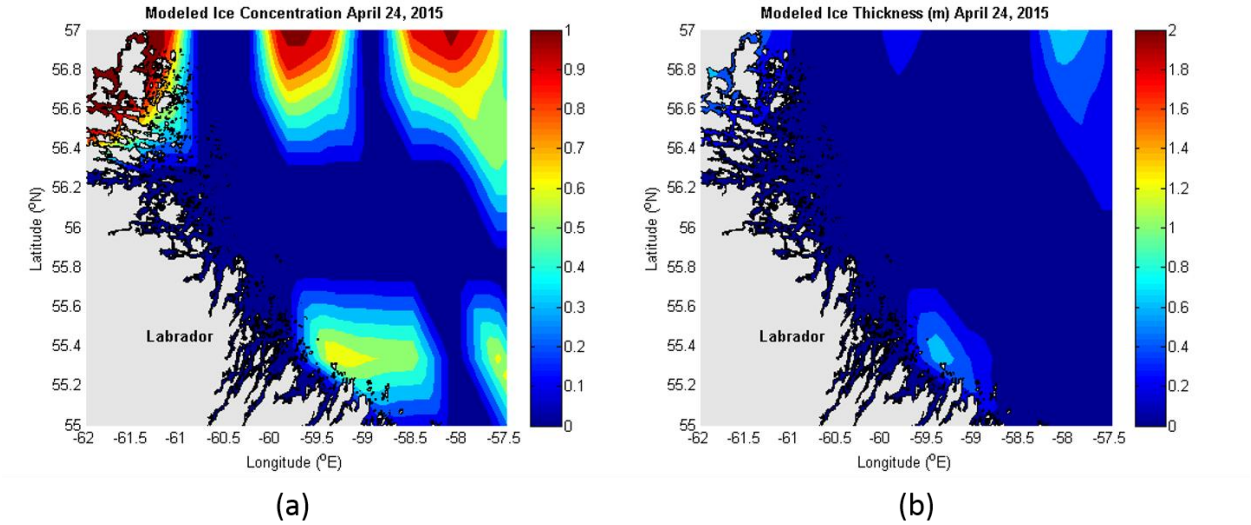

774

775 **Figure 20.** Sea ice concentration (a) and thickness (b) on April 24, 2015 03:00 UTC (00:00 AST) from the
776 thermodynamic model with no initial snow cover.

777 Figure 21-Figure 23 show contour plots of the modeled and LIM2 ice thickness and concentration across the model
778 domain for May 2, 3, and 7, respectively. These dates were selected to coincide with the timing of the first detected
779 motion of the land-fast ice buoys deployed offshore Nain. These buoys began to drift on May 1, 2, and 6. The model
780 results shown here are all from the run initialized with 0.4 m of snow cover. While the modeled results and LIM2
781 data show somewhat different patterns of ice retreat during the May 2-7 period, both show a general pattern of the
782 retreat of thicker, more concentrated ice toward the northern end of the model domain.

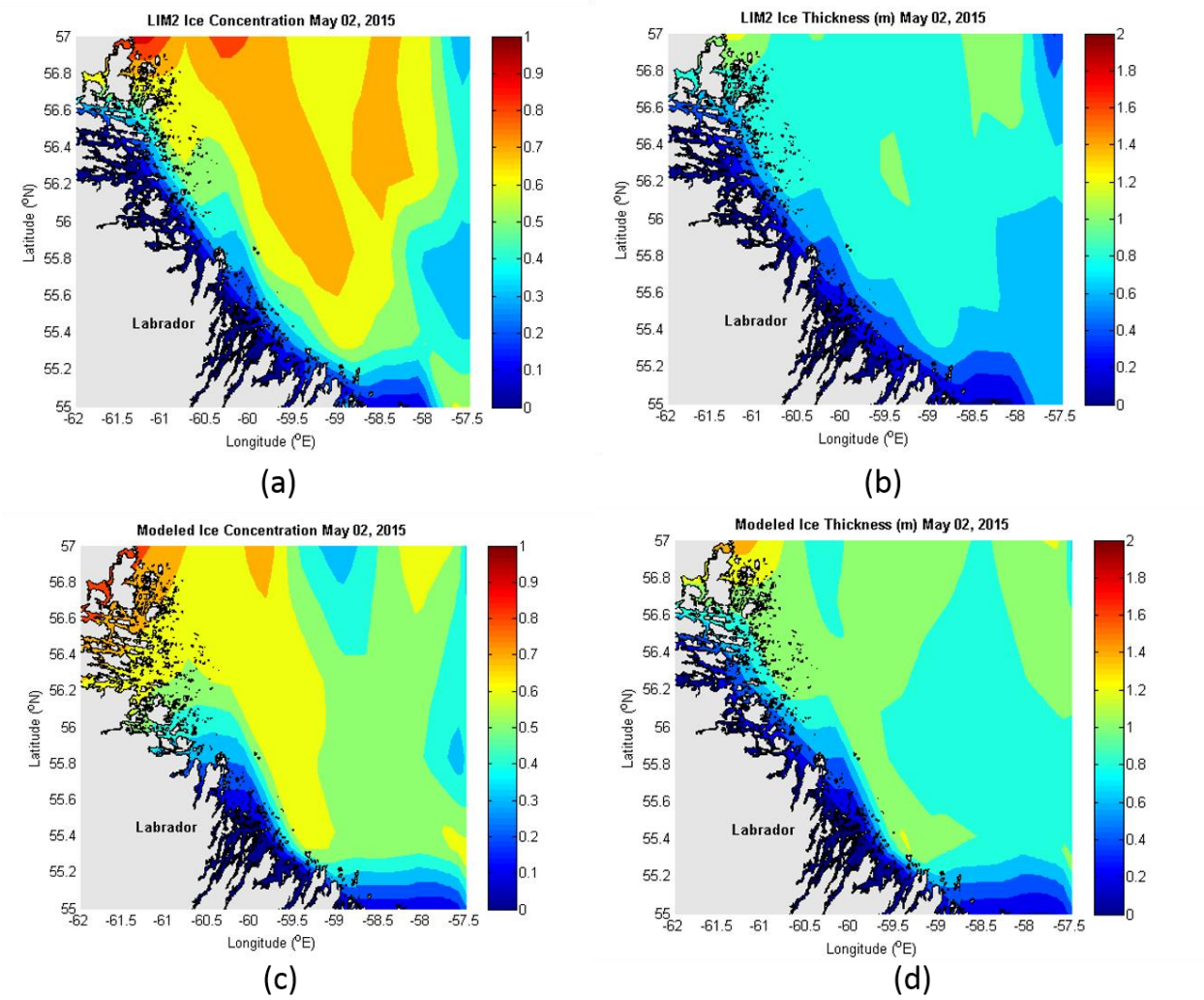

783

784 **Figure 21.** Sea ice concentration (a,c) and thickness (b,d) on May 02, 2015 03:00 UTC (00:00 AST) from LIM2
785 data (a,b) and the thermodynamic model presented here (c,d). The results of the thermodynamic model run shown
786 here are initialized with 40 cm of snow.

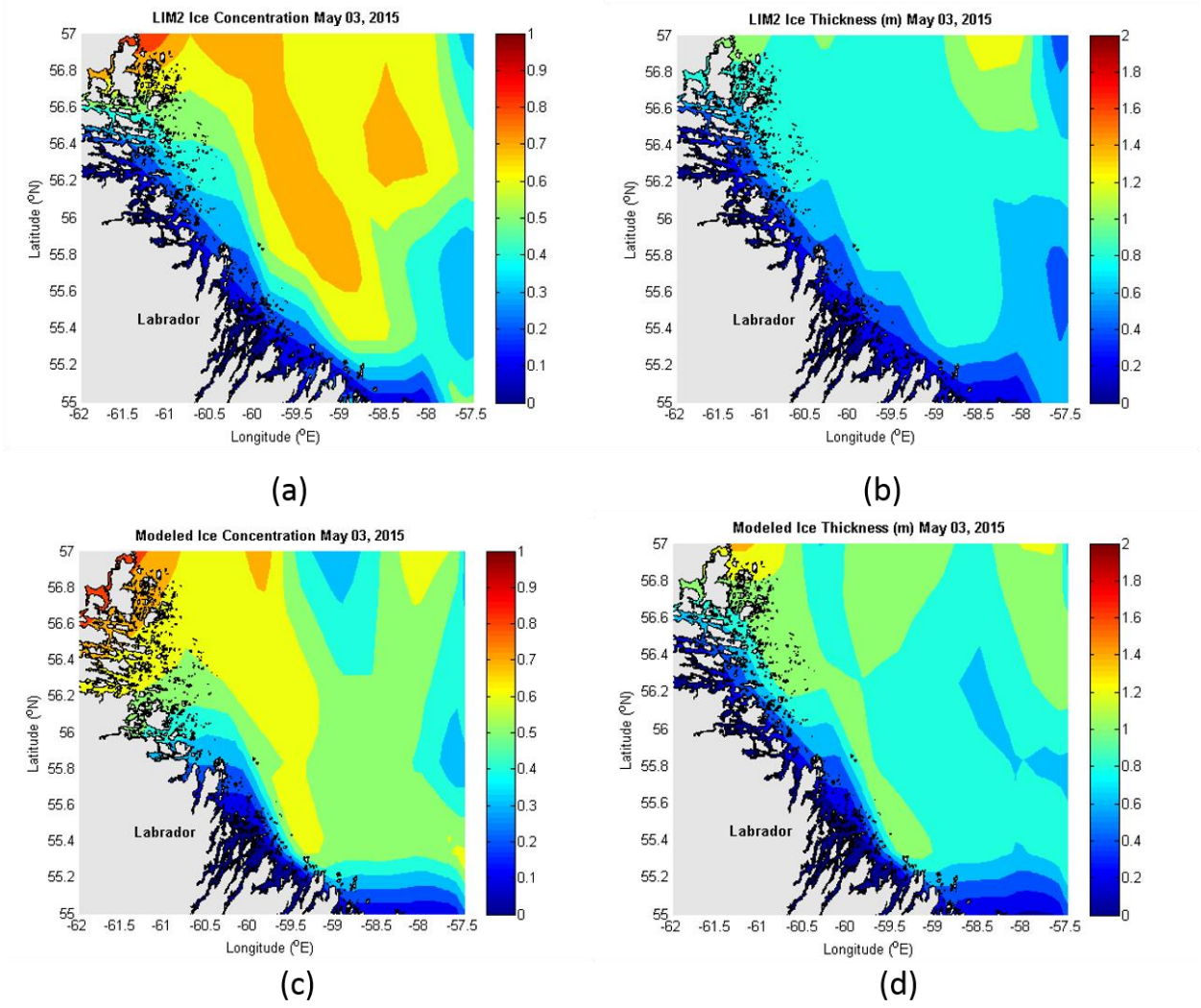

Figure 22. Sea ice concentration (a,c) and thickness (b,d) on May 03, 2015 03:00 UTC (00:00 AST) from LIM2 data (a,b) and the thermodynamic model presented here (c,d). The results of the thermodynamic model run shown here are initialized with 40 cm of snow.

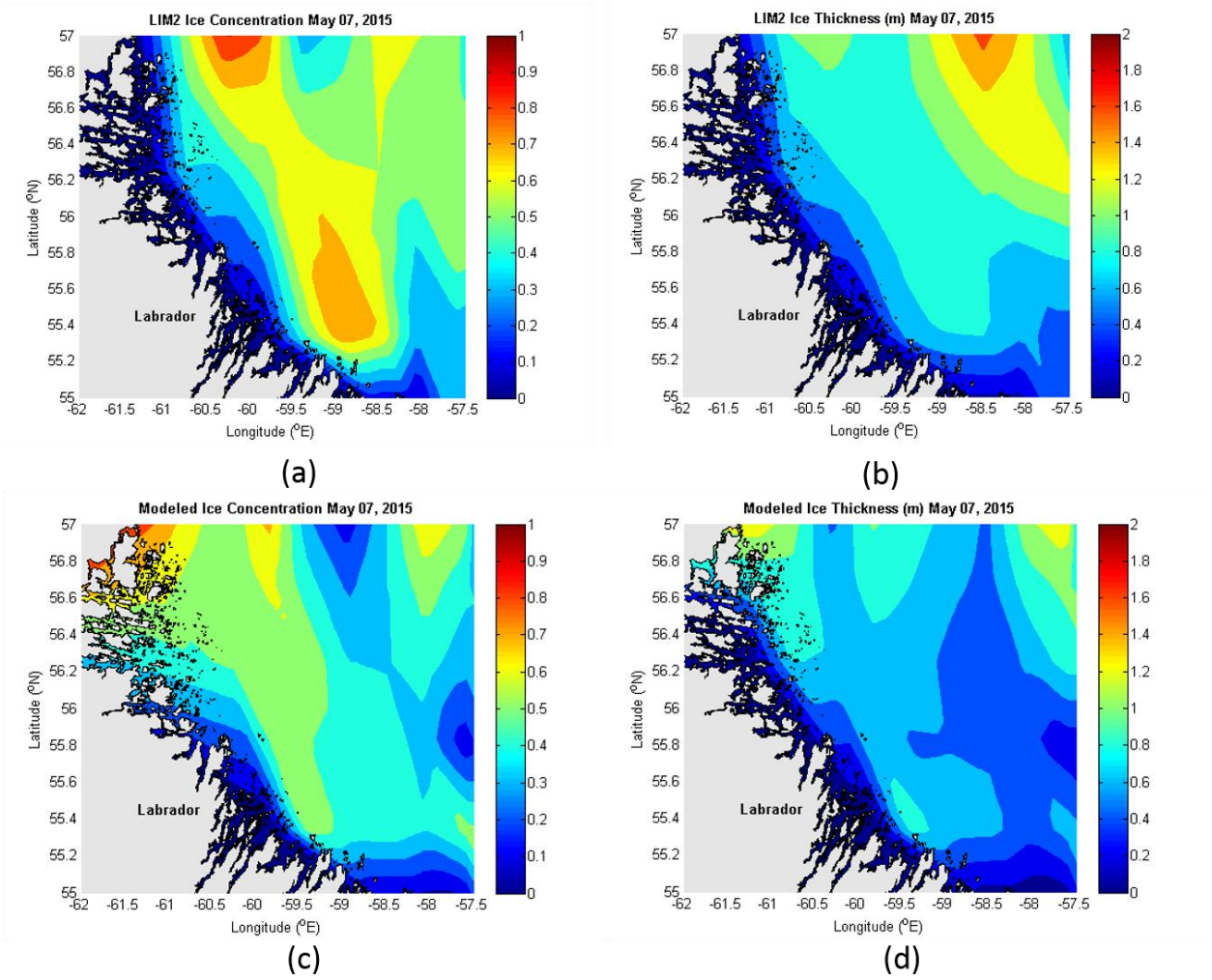

Figure 23. Sea ice concentration (a,c) and thickness (b,d) on May 07, 2015 03:00 UTC (00:00 AST) from LIM2 data (a,b) and the thermodynamic model presented here (c,d). The results of the thermodynamic model run shown here are initialized with 40 cm of snow.

Figure 24 shows the evolution of average ice conditions during April 1 – May 31, 2015 over the model domain according to the LIM2 data, the thermodynamic model with 40 cm of initial snow cover, and the thermodynamic model with no initial snow cover. The spatially averaged ice thickness and concentration for the model run with 0.4 m of initial snow cover tracks closely to the LIM2 mean thickness and concentration, and begins to decrease significantly on May 11 when both the mean thickness and concentration decrease to less than 0.5 (m or concentration). The ice disappears completely from the model domain on May 15. The spatially averaged ice thickness and concentration for the model run with no initial snow cover tracks closely to the LIM2 mean thickness and concentration, and begins to decrease significantly on April 21 when both the mean thickness and concentration decrease to less than 0.5 (m or concentration). In the model run with no initial snow cover, the ice disappears completely on May 1. The LIM2 mean domain ice thickness and concentration both remain fairly constant around

0.6 (m or concentration) during April 1 – May 11, and subsequently begin to display greater variability between 0.3-0.7 (m or concentration) while showing an overall decrease, until May 31.

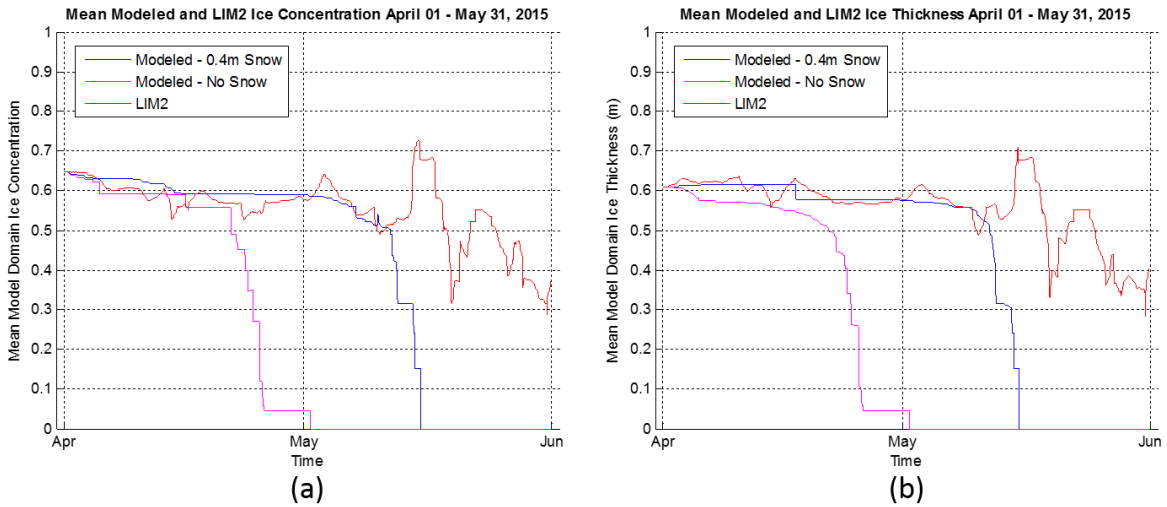

Figure 24. Evolution of average ice concentration (a) and thickness (b) over the entire model domain during April 1 – May 31, 2015. The red lines represent LIM2 ice conditions, the blue lines represent ice conditions for the thermodynamic model presented here initialized with 40 cm of snow, and the magenta lines represent ice conditions for the thermodynamic model initialized with no snow.

Table 5 summarizes the model domain mean ice thicknesses and concentrations for the selected dates shown in Figure 19-Figure 23 for the LIM2 dataset, the model run with 0.4 m of initial snow cover, and the model run with no initial snow cover.

Table 5. Summary of modeled vs. LIM2 model domain mean ice concentration and thickness for selected dates for April 1 – May 31, 2015 model run.

Modeled vs. LIM2 Mean Domain Ice Concentration and Thickness (Thermodynamic Model)					
Date	**April 01 Snow Cover (m)**	**LIM2 Concentration**	**Modeled Concentration**	**LIM2 Thickness (m)**	**Modeled Thickness (m)**
April 24	0.40	0.42	0.57	0.43	0.48
	0.00		0.44		0.43
May 02	0.40	0.77	0.54	0.65	0.47
	0.00		0.00		0.00
May 03	0.40	0.78	0.53	0.69	0.47
	0.00		0.00		0.00

May 07	0.40	0.36	0.46	0.39	0.45
	0.00		0.00		0.00

817

818 **3.2 Thermodynamic-dynamic model results**

819 The coupled thermodynamic-dynamic model run for May 1-7, 2015 is initialized with the LIM2 ice thickness,
820 concentration, and velocity grid for May 1 00:00 UTC (Figure 25). The green circle represents the single coordinate
821 offshore Makkovik analyzed here (55.25°N, 59.25°W), and the purple circle represents the coordinate offshore Nain
822 (56.5°N, 61°W). Given that the ice particles are free to drift from their initial positions in the dynamic model, the
823 modeled ice conditions at these coordinates are linearly interpolated.

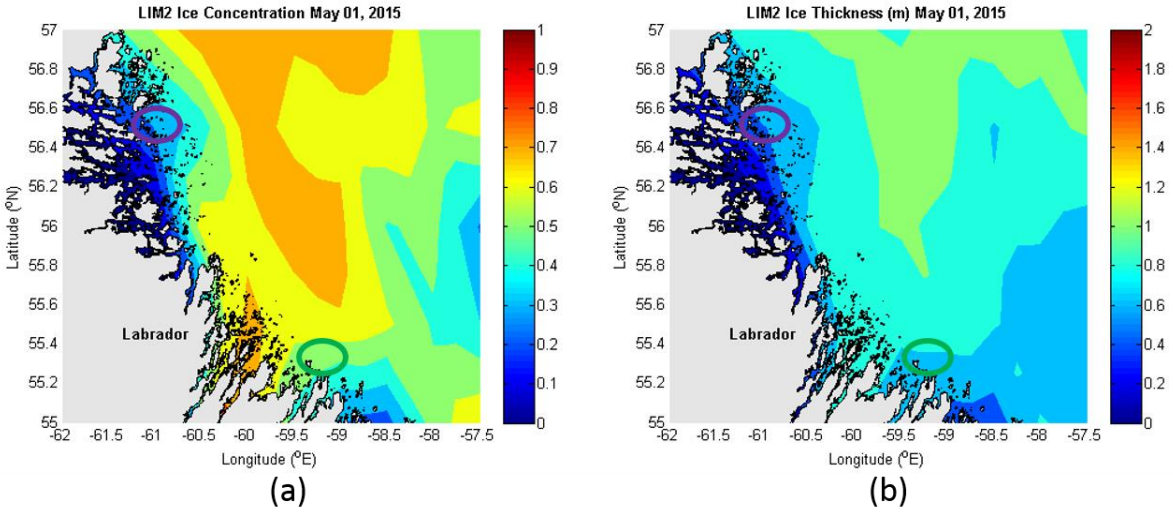

824

825 **Figure 25.** Sea ice concentration (a) and thickness (b) over the model domain at the start of the thermodynamic-
826 dynamic model run on May 1, 2015 00:00 UTC, as obtained from the LIM2 dataset. The region circled in green
827 represents the area over which ice conditions offshore Makkovik are analyzed in this section, and the purple circled
828 region represents the area over which ice conditions offshore Nain are analyzed.

829 Figure 26 shows the evolution of modeled and the LIM2 ice thickness (a,c) and concentration (b,d) during May 1-7
830 offshore Makkovik (a,b) and Nain (c,d).

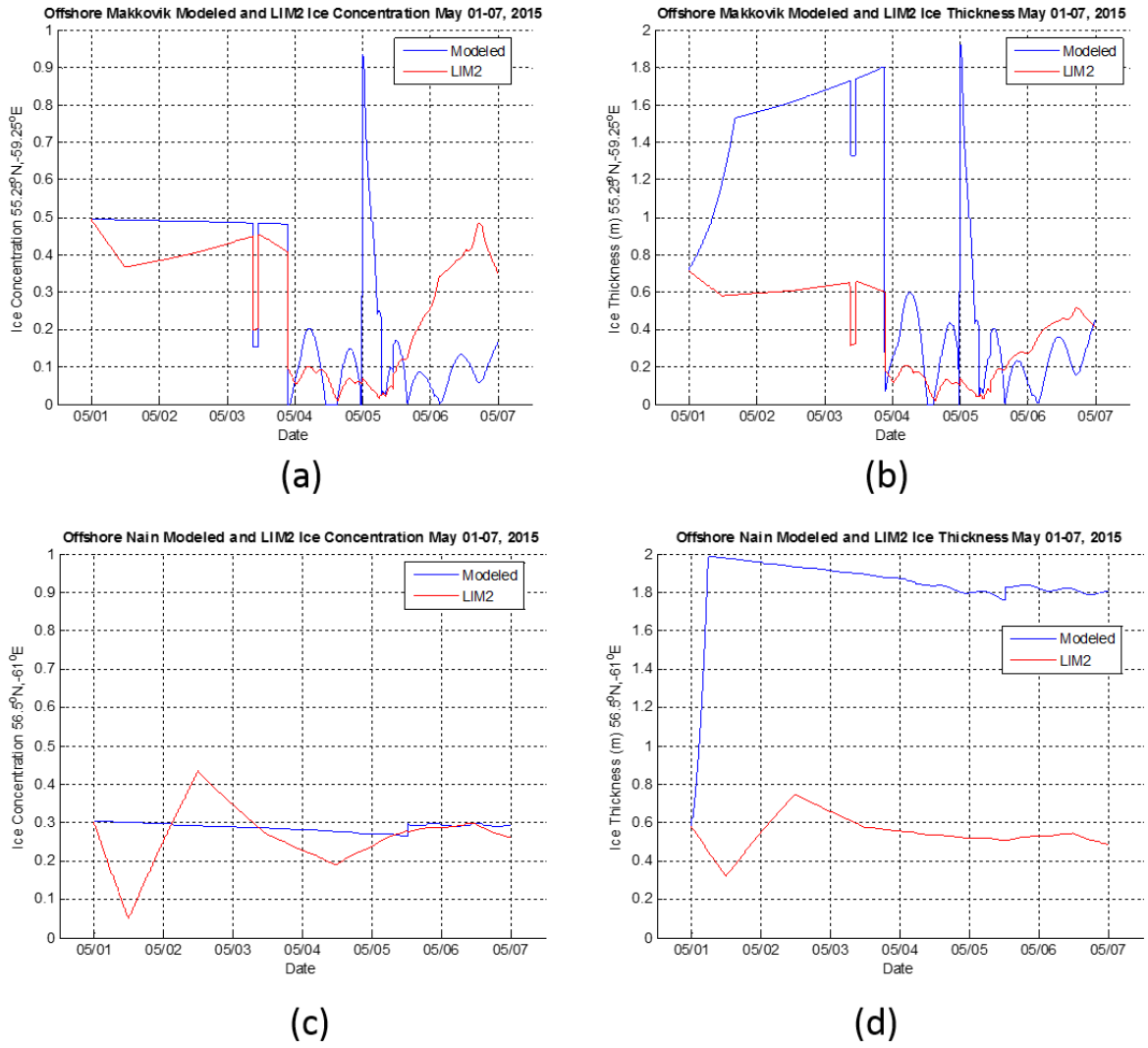

831

832 **Figure 26.** Evolution of average ice concentration (a,c) and thickness (b,d) in the focus regions offshore Makkovik
833 (a,b) and Nain (c,d) during May 1-7, 2015. The red lines represent LIM2 ice conditions, and the blue lines represent
834 ice conditions for the thermodynamic-dynamic model. The latitude-longitude coordinates shown on the y-axes
835 represent the central locations for the regions over which average ice conditions are shown.

836 Figure 27-Figure 30 show the modeled ice drift velocities and total speeds along the trajectories of buoys 1-4 during
837 May 1-7. The plots for buoy 4 begin on May 2 when the buoy began to record drift (Figure 30). Results for buoys 5-
838 6 are not shown because buoy 5 remained stationary on the land-fast ice offshore Makkovik for its entire
839 transmission period, and buoy 6 did not drift for more than 24 hours during the model run period. The results show
840 that the model can reproduce mean regional ice drift velocities; however the model tends to underestimate high-
841 frequency spikes in drift speeds compared to those recorded by the drift buoys 1 and 4 (Figure 27 and Figure 30).
842 Along the track of buoy 1, the model does not capture the tidally-forced oscillations in the ice drift velocity as
843 recorded by the buoy; this is most likely due to the inadequate spatial resolution of the NEMO 3.1 ocean current

input. For the along-track drift speeds of buoys 2 and 3, the model overestimates the increase in ice drift speeds during May 3-7 (Figure 28-Figure 29).

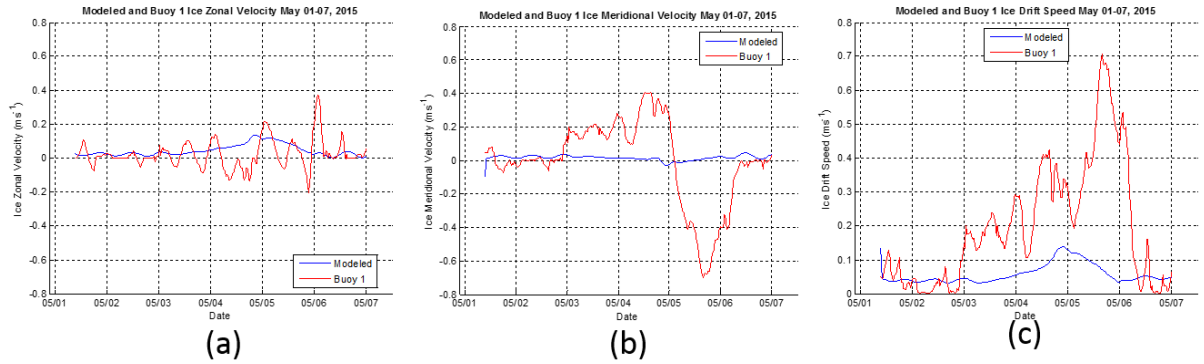

Figure 27. Modeled (blue lines) and buoy 1 measured (red lines) along-track ice drift zonal (a), meridional (b) velocities, and speeds (c) during May 1-7, 2015 offshore Labrador.

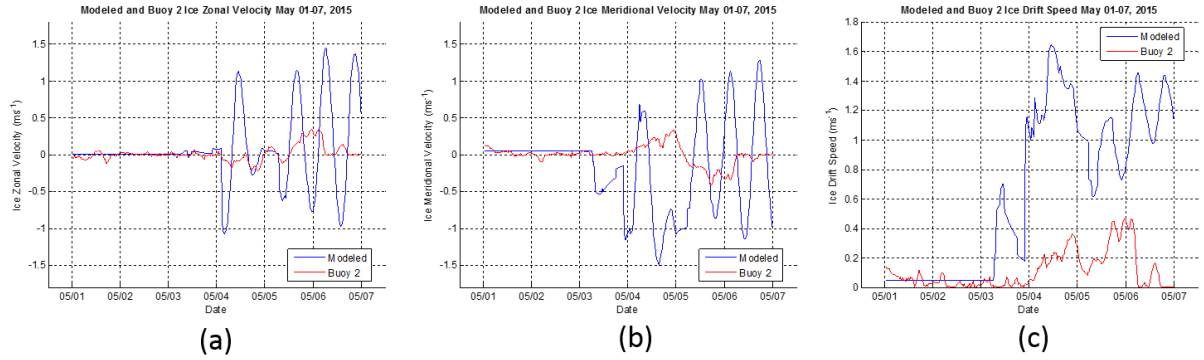

Figure 28. Modeled (blue lines) and buoy 2 measured (red lines) along-track ice drift zonal (a), meridional (b) velocities, and speeds (c) during May 1-7, 2015 offshore Labrador.

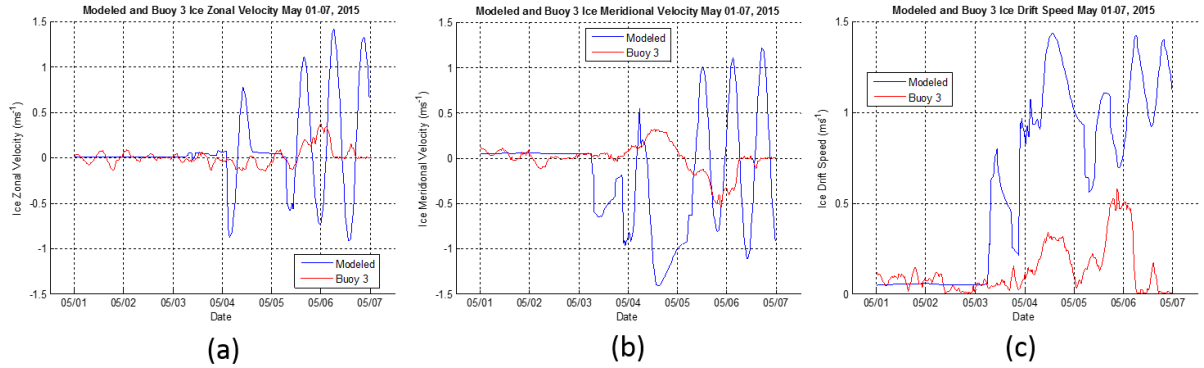

Figure 29. Modeled (blue lines) and buoy 3 measured (red lines) along-track ice drift zonal (a), meridional (b) velocities, and speeds (c) during May 1-7, 2015 offshore Labrador.

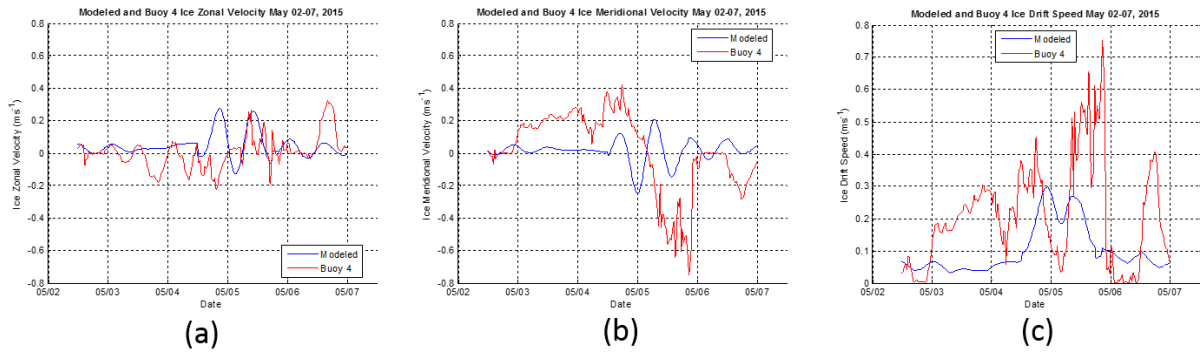

Figure 30. Modeled (blue lines) and buoy 4 measured (red lines) along-track ice drift zonal (a), meridional (b) velocities, and speeds (c) during May 1-7, 2015 offshore Labrador.

Figure 31 shows the observed minus modeled ice drift speed errors during May 1-7 for buoys 1-4. The buoy-recorded and modeled drift speeds were very close during May 1-3. For buoys 1 and 4, the observed-modeled drift speed error increases to 0.2-0.5 m s^{-1} during May 3-7. For buoys 2 and 3, the observed-modeled drift speed error increases to 0.5-1.5 m s^{-1} during this same period. These results indicate that the model is better at simulating observed ice drift speeds further offshore compared to nearshore drift speeds, as buoys 1 and 4 drifted further offshore than buoys 2 and 3 (see Figure 1). Beginning on May 3, the modeled ice velocities along the tracks of buoys 2 and 3 increase significantly over the observed buoy-tracked ice velocities. This is due to increases in the internal ice stresses, sea surface tilt forcing, and coastal boundary forcing along the nearshore tracks of buoys 2 and 3 in the model.

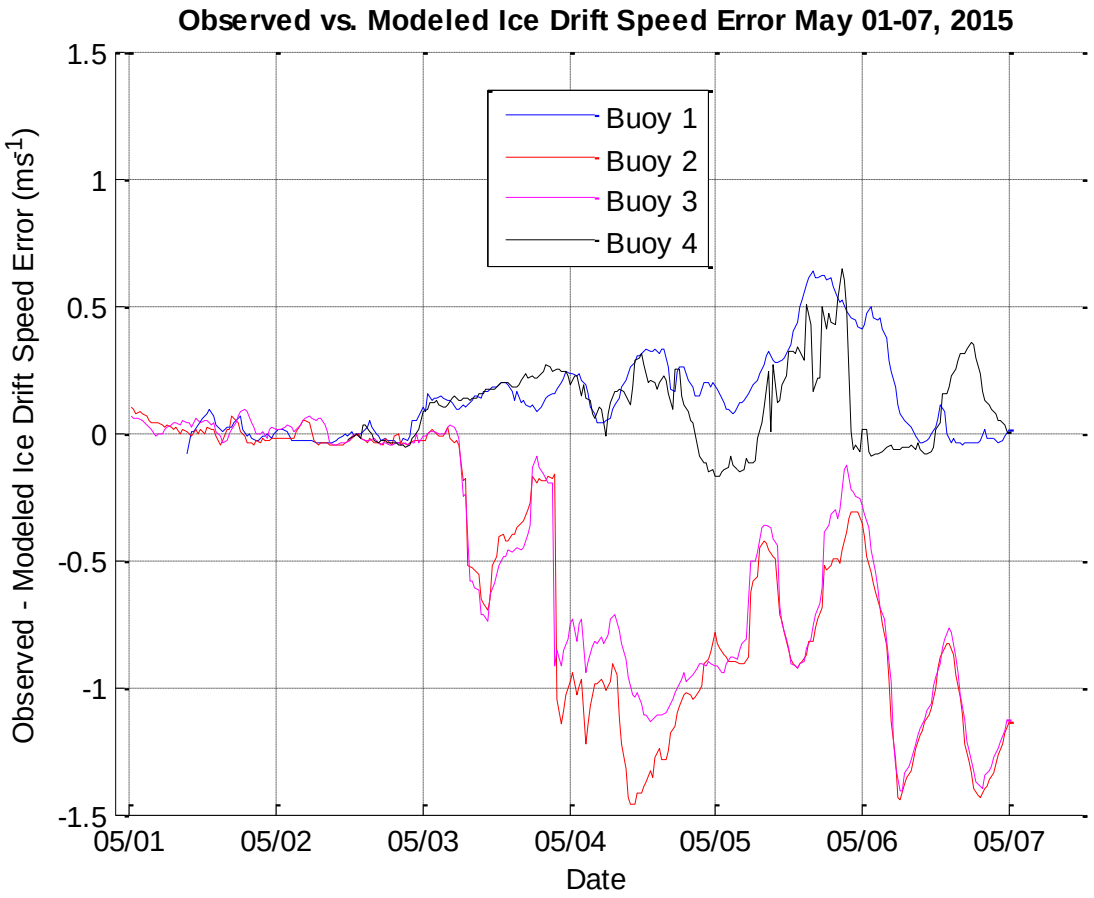

867

868 **Figure 31.** Observed minus modeled ice drift speeds along the trajectories of buoys 1-4 during May 1-7, 2015
869 offshore Labrador.

870 Figure 32-Figure 34 show the LIM2 and modeled ice thickness and concentrations for the model domain for May 3,
871 5, and 7, respectively. The model tends to overestimate ice thicknesses and concentrations across the domain;
872 however the model does capture the fact that a tongue of higher ice concentrations develops toward the middle of
873 the model domain.

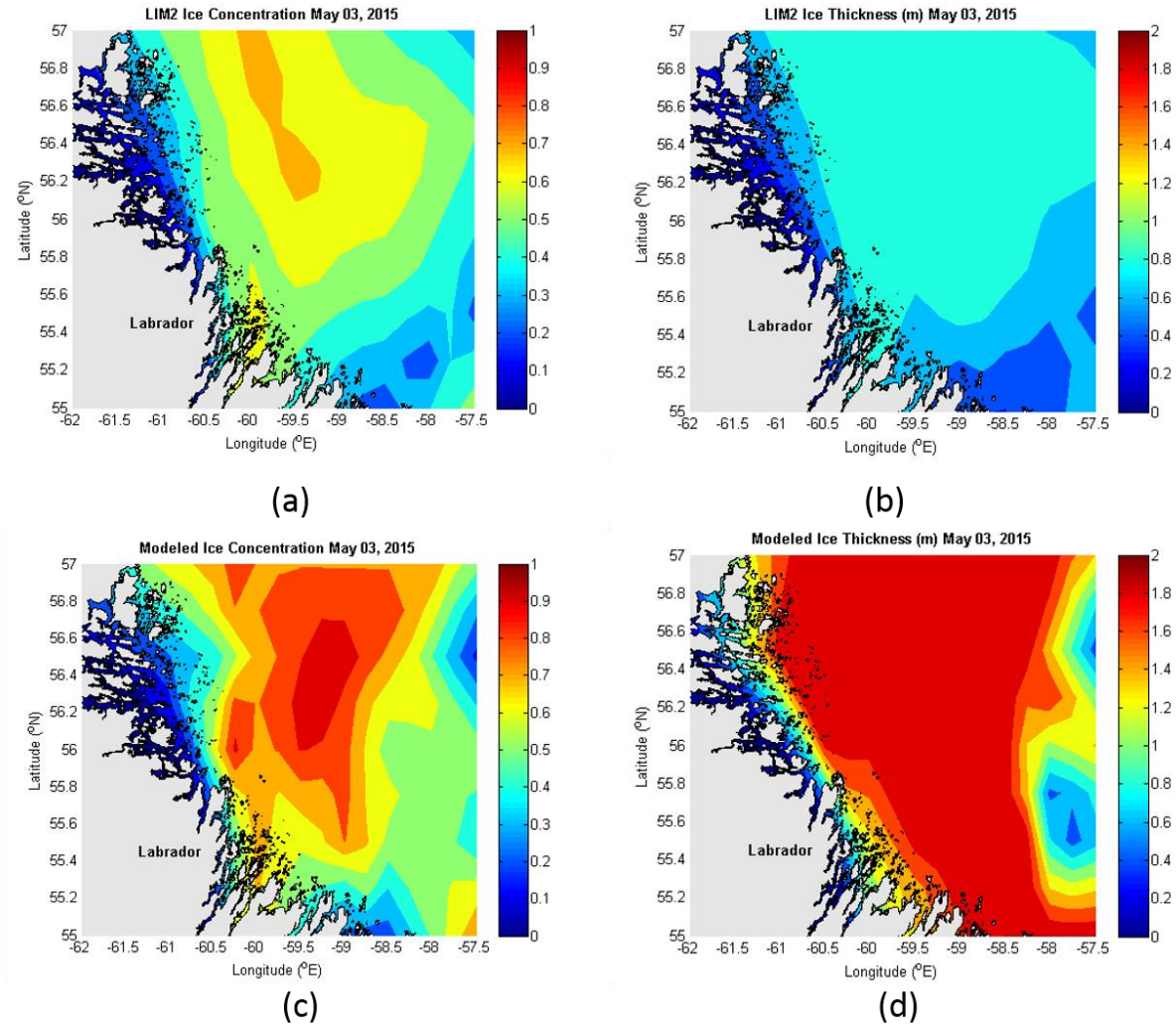

874

875 **Figure 32.** Sea ice concentration (a,c) and thickness (b,d) on May 03, 2015 03:00 UTC (00:00 AST) from LIM2
876 data (a,b) and the thermodynamic-dynamic model presented here (c,d).

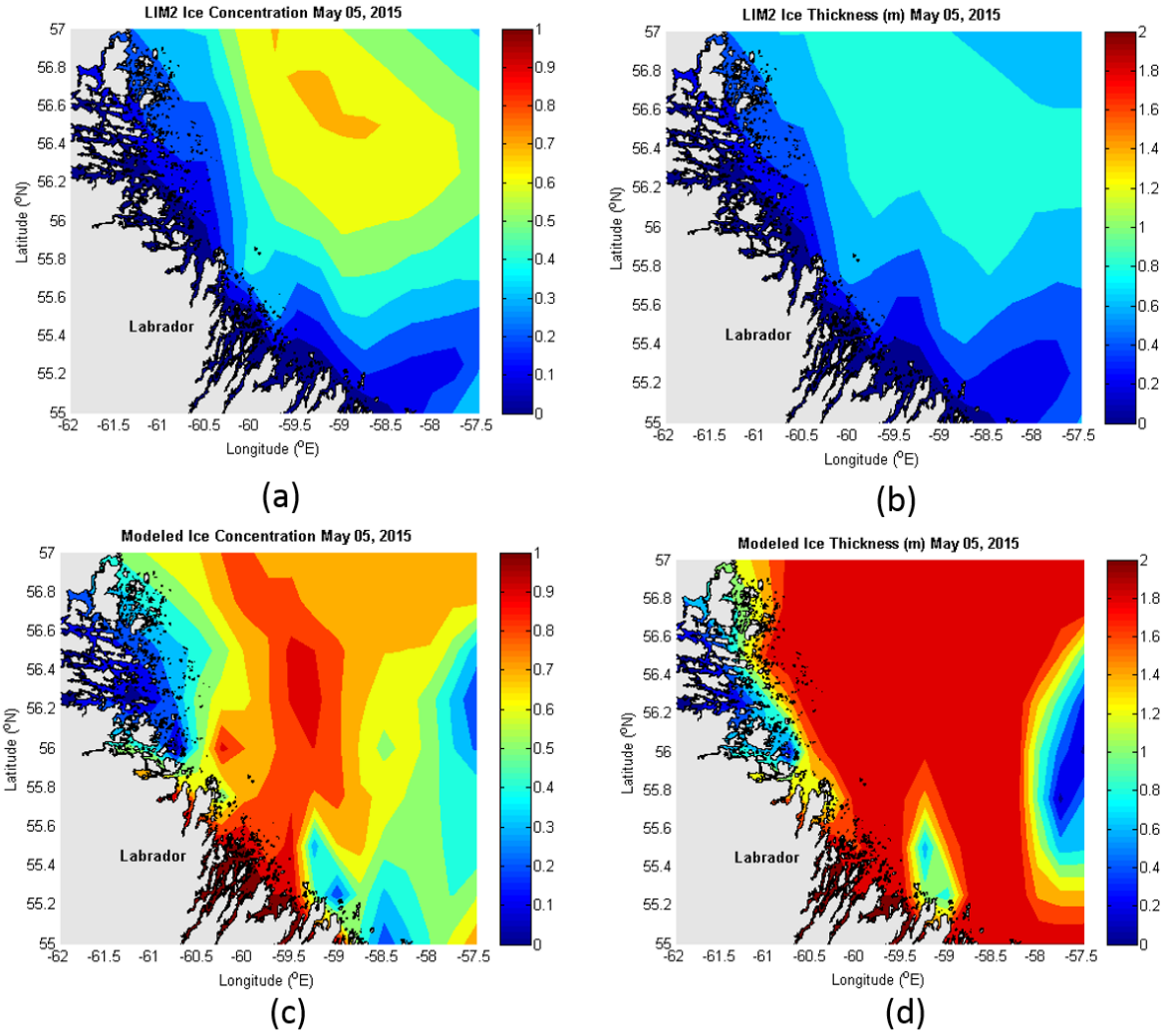

877

878 **Figure 33.** Sea ice concentration (a,c) and thickness (b,d) on May 05, 2015 03:00 UTC (00:00 AST) from LIM2
879 data (a,b) and the thermodynamic-dynamic model presented here (c,d).

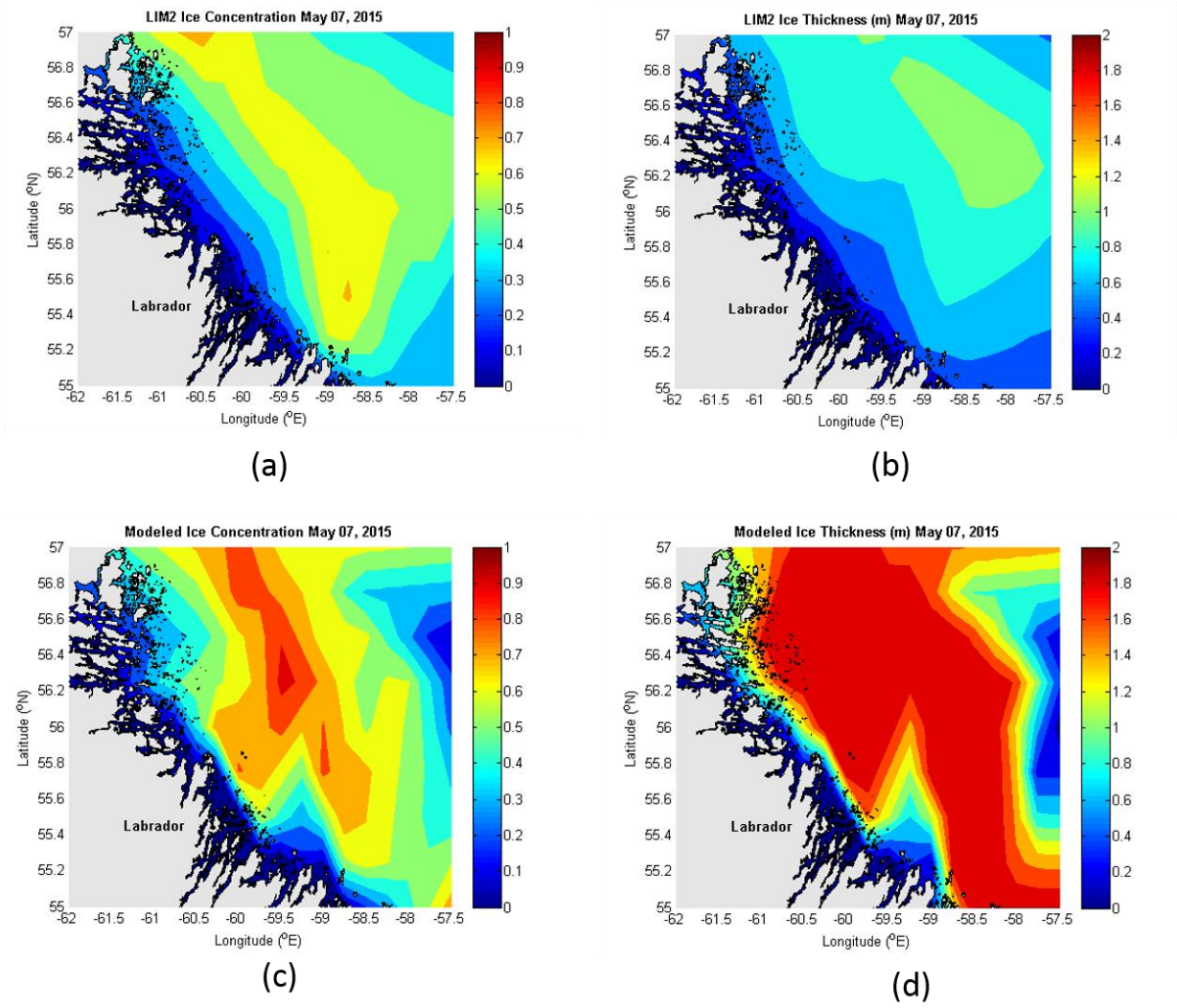

880

881 **Figure 34.** Sea ice concentration (a,c) and thickness (b,d) on May 07, 2015 00:00 UTC (May 06 21:00 AST) from
882 LIM2 data (a,b) and the thermodynamic-dynamic model presented here (c,d).

883 Figure 35 shows the evolution of the mean model domain ice thickness (a) and concentration (b) during May 1-7 for
884 the model and the LIM2 dataset.

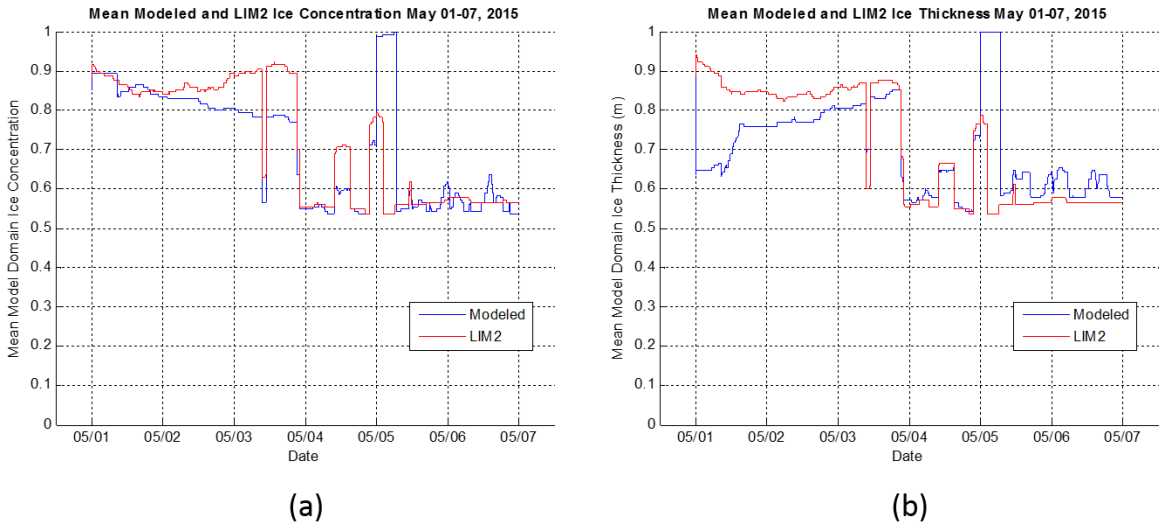

885

886 **Figure 35.** Evolution of average ice concentration (a) and thickness (b) over the entire model domain during May 1-
887 7, 2015. The red lines represent LIM2 ice conditions, and the blue lines represent ice conditions for the
888 thermodynamic-dynamic model presented here.

889 Table 6 summarizes the mean model domain ice thicknesses and concentrations for the model and the LIM2 dataset
890 for the selected dates analyzed in this section.

891 **Table 6.** Summary of modeled vs. LIM2 model domain mean ice concentration and thickness for selected dates for
892 May 1-7, 2015 model run.

Modeled vs. LIM2 Mean Domain Ice Concentration and Thickness (Thermodynamic-Dynamic Model)				
Date	**LIM2 Concentration**	**Modeled Concentration**	**LIM2 Thickness (m)**	**Modeled Thickness (m)**
May 03	0.55	0.78	0.54	0.81
May 05	0.42	0.75	0.42	0.80
May 07	0.39	0.55	0.38	0.79

893 **4 Conclusions**

894 A model is presented in this paper which can be used to generate short-term (several days) to seasonal (months)
895 forecasts of regional ice conditions for coastal Labrador. It was shown that when the thermodynamic model was
896 used by itself for the April-May 2015 period, forecasts of the timing of the near-disappearance of ice near Makkovik
897 and Nain, Labrador were accurate to within one to four days when the model was initialized on April 1 (Figure 17).
898 For the specific locations on the land-fast ice at which the tracking buoys were originally deployed, the
899 thermodynamic model predicted the times at which the land-fast ice started to break-up accurately to within 4.7
900 hours to up to almost six days (Figure 18 and Table 4). However, these model results assumed a uniform snow cover

of 0.4 m on the sea ice on April 1 for the whole model domain of coastal Labrador. Given the extreme uncertainty of this initial condition, it is imperative that operational use of this model utilize accurate measurements of snow cover for the initialization of the model. It may be possible to hindcast initial snow depths by fitting the thermodynamic model to seasonal evolutions of ice cover as documented by the CIS ice charts.

The thermodynamic model can be used to generate seasonal forecasts of the timing and spatial pattern of the break-up of the land-fast ice along coastal Labrador. Such forecasts are important to operational planning for possible future oil and gas exploration and production operations in this region, as well as vessel transport operations such as those associated with the Voisey's Bay nickel mine. Access to ports near Makkovik and Nain is not possible for low or non-ice class vessels prior to the break-up of the land-fast ice.

The coupled thermodynamic-dynamic model can be used to issue forecasts of the evolution of the coastal Labrador ice cover over shorter periods of days to weeks compared to the thermodynamic-only model, which can help inform the planning of ice management operations and vessel routing. The modeled ice drift speeds during May 1-7, 2015 were within 1.5 m s^{-1} of those measured by the tracking buoys deployed on the land-fast ice during April (Figure 31). Given the fact that the dynamic model does not account for ice entering or leaving the edges of the model domain, the model should be run for as large an area as possible and for shorter periods, with the selected model domain boundaries far away from particular locations of interest for ice forecasting. The temporal and spatial resolution of the model can be adjusted by the user, with computational efficiency and model runtimes improving at lower resolutions.

The model is most likely sensitive to a number of the thermodynamic and dynamic parameters such as the number of nearest-neighbor ice particles and the smoothing length used in the SPH scheme, among others. Further study of the model's sensitivity to these parameters is warranted. In addition, the thermodynamic model for prediction of the onset of land-fast ice break-up does not account for the effects of wind stress. The wind speed in the current thermodynamic model only affects the ice through the sensible and latent heat fluxes (Eqs. 32 and 39, respectively). Future development of this model should account for the tensile stresses imposed on the offshore land-fast ice boundary by the offshore component of the wind.

Finally, it is important to note that the results shown in this paper were generated with observed and hindcast metocean data. Operational use of this model will require forecast metocean data, which will increase the errors in the ice forecasts. However, the model can be reinitialized in near-real-time with the most up-to-date locally observed gridded ice and metocean datasets in order to improve regional ice forecasts. Export of this model to other ice environments is also an important aspect of this model development effort.

Code and Data Availability

Upon request to the lead author, the ice buoy drift data and model output raw data can be provided. The model code is proprietary to C-CORE; however, for the review process, the model code can be made available temporarily to the

reviewers and journal editor. Upon request, all materials will be uploaded to a C-CORE FTP site with login details provided.

Author Contributions

Ian Turnbull led the deployment of the ice tracking buoys, developed the model code, ran the simulations, and wrote the paper. Rocky Taylor assisted with the deployment of the ice tracking buoys and helped revise the paper.

Competing Interests

The authors declare that they have no conflicts of interest.

Acknowledgments

We thank Innu Mikun Airlines of Happy Valley-Goose Bay, NL for providing safe and reliable charter aircraft services for the deployment of the ice tracking buoys. The authors gratefully acknowledge core funding for the Centre for Arctic Resource Development (CARD) program at C-CORE by Hibernia Management and Development Company, Ltd. (HMDC), the Terra Nova Development (Suncor Energy, Inc. – Operator), and the Research and Development Corporation (RDC) of Newfoundland and Labrador. Additional financial support from RDC for aspects of this work is gratefully acknowledged. Finally, we thank Dr. Martin Richard of C-CORE for his helpful advice on constructing the ice model. The ice drift buoy and model output datasets used in this paper can be obtained by request from the corresponding author. The model computer code is proprietary to C-CORE and cannot be made publicly available.

References

Canadian Coast Guard (CCG) (2013), Chapter 3: Ice Climatology and Environmental Conditions. Accessed on the World Wide Web: http://www.ccg-gcc.gc.ca/Icebreaking/Ice-Navigation-Canadian-Waters/Ice-Climatology-and-Environmental-Conditions, March 8, 2016.

Canadian Ice Service (CIS) Weekly Digital Ice Charts (2016), Accessed on the World Wide Web: http://iceweb1.cis.ec.gc.ca/Archive/page1.xhtml;jsessionid=E8B1CC6854F560205EDA89C07D6D15F7?lang=en, April 27, 2016.

Cooke, M.A., Demirov, E., and Zhu, J. (2014), A Model Study of the Relationship between Sea-Ice Variability and Surface and Intermediate Water Mass Properties in the Labrador Sea, Atmosphere-Ocean, 52(2), 142-154.

Davis, C.H. (1996), Temporal Change in the Extinction Coefficient of Snow on the Greenland Ice Sheet from an Analysis of Seasat and Geosat Altimeter Data, IEEE Transactions on Geoscience and Remote Sensing, 34(5), 1,066-1,073.

963 Ebert, E.E., and Curry, J.A. (1993), An Intermediate One-Dimensional Thermodynamic Sea Ice Model for
964 Investigating Ice-Atmosphere Interactions, Journal of Geophysical Research, 98(C6), 10,085-10,109.

965 European Center for Medium-Range Weather Forecasting (ECMWF), ERA-Interim Reanalysis, Accessed on the
966 World Wide Web: http://apps.ecmwf.int/datasets/data/interim-full-daily/levtype=sfc/, March 8, 2016.

967 Food and Agriculture Organization (FAO) of the United Nations (2015), Chapter 3 – Meteorological data. Accessed
968 on the World Wide Web: http://www.fao.org/docrep/x0490e/x0490e07.htm, March 8, 2016.

969 Fenty, I., and Heimbach, P. (2013), Coupled Sea-Ice-Ocean-State Estimation in the Labrador Sea and Baffin Bay,
970 Journal of Physical Oceanography, 43(5), 884-904.

971 Fofonoff, N.P., and Millard Jr., R.C. (1983), Algorithms for computation of fundamental properties of seawater,
972 Unesco technical papers in marine science, 44.

973 General Bathymetric Chart of the Oceans (GEBCO) (2008), Accessed on the World Wide Web:
974 http://www.gebco.net/data_and_products/gridded_bathymetry_data/, March 8, 2016.

975 Global Ocean 1/12° Physics Analysis and Forecast, Accessed on the World Wide Web:
976 http://marine.copernicus.eu/web/69-interactive-
977 catalogue.php?option=com_csw&view=details&product_id=GLOBAL_ANALYSIS_FORECAST_PHYS_
978 001_002, March 8, 2016.

979 Gutfraind, R., and Savage, S.B. (1997), Smoothed Particle Hydrodynamics for the Simulation of Broken-Ice Fields:
980 Mohr-Coulomb-Type Rheology and Frictional Boundary Conditions, Journal of Computational Physics,
981 134, 203-215.

982 Hibler III, W.D. (1979), A Dynamic Thermodynamic Sea Ice Model, Journal of Physical Oceanography, 9, 815-846.

983 Holland, M.M., Bailey, D.A., Briegleb, B.P., Light, B., and Hunke, E. (2012), Improved Sea Ice Shortwave
984 Radiation Physics in CCSM4: The Impact of Melt Ponds and Aerosols on Arctic Sea Ice, Journal of
985 Climate, 25, 1,413-1,430.

986 International Standards Organization Draft International Standard (ISO/DIS 19901-1) (2013), Petroleum and natural
987 gas industries – Specific requirements for offshore structures – Part 1: Metocean design and operating
988 considerations.

989 Khandekar, M.L. (1980), Inertial oscillations in floe motion over the Beaufort Sea – observations and analysis,
990 Atmosphere-Ocean, 18(1), 1-14.

991 Konig-Langlo, G., and Augstein, E. (1994), Parameterization of the downward long-wave radiation at the Earth's
992 surface in polar regions, Meteorologische zeitschrift, N.F.3, Jg. 1994, H.6, 343-347.

993 Lazier, J.R.N., and Wright, D.G. (1993), Annual Velocity Variations in the Labrador Current, Journal of Physical
994 Oceanography, 23, 659-678.

995 Lindsay, R.W., and Stern, H.L. (2004), A New Lagrangian Model of Arctic Sea Ice, Journal of Physical
996 Oceanography, 34, 272-283.

997 MacKinnon, A. (2015), The Dufort-Frankel Method. Accessed on the World Wide Web:
998 http://www.cmth.ph.ic.ac.uk/people/a.mackinnon/Lectures/compphys/node35.html, March 8, 2016.

999 Matthews, J.H., and Fink, K.K. (2004), Numerical methods using Matlab, 4th Edition, Prentice-Hall, Inc., Upper
1000 Saddle River, New Jersey, USA 0-13-065248-2, 505-508.

1001 Maykut, G.A., and Untersteiner, N. (1971), Some results from a time dependent thermodynamic model of sea ice,
1002 Journal of Geophysical Research, 76, 1,550-1,575.

1003 Mitchell, A.R., and Griffiths, D.F. (1980), The Finite Difference Method in Partial Differential Equations, John
1004 Wiley, New York, USA.

1005 National Oceanographic and Atmospheric Administration (NOAA) (2015), General Solar Position Calculations.
1006 Accessed on the World Wide Web: http://www.esrl.noaa.gov/gmd/grad/solcalc/solareqns.PDF, March 8,
1007 2016.

1008 North American Regional Reanalysis (NARR), NCEP Reanalysis data provided by the NOAA/OAR/ESRL PSD,
1009 Boulder, Colorado, USA, from their Web site at http://www.esrl.noaa.gov/psd/, March 8, 2016.

1010 Peng, S. (1989), Application of a Simple Ice-Ocean Model to the Labrador Sea. Master of Science Thesis,
1011 Department of Meteorology, McGill University, Montreal, Quebec, Canada.

1012 Prinsenberg, S.J., Peterson, I.K., Holladay, J.S., and Lalumiere, L. (2011), Snow and Ice Thickness Properties of
1013 Lake Melville, a Canadian Fjord Located along the Labrador Coast, Proceedings of the Twenty-first (2011)
1014 International Offshore and Polar Engineering Conference (ISOPE), Maui, Hawaii, USA, June 19-24, 2011.

1015 Prinsenberg, S.J., and Yao, Q. (1999), The Seasonal Evolution of Sea Ice Cover off eastern Canada as Simulated by
1016 a Coupled Ice-Ocean Model for 1991/92 and Expected $2\times CO_2$ atmospheric conditions. Accessed on the
1017 World Wide Web: http://www.bio.gc.ca/science/research-recherche/ocean/ice-
1018 glace/documents/prins05.pdf, March 8, 2016.

1019 Sayed, M., Carrieres, T., Tran, H., and Savage, S.B. (2002), Development of an Operational Ice Dynamics Model
1020 for the Canadian Ice Service, Proceedings of the Twelfth (2002) International Offshore and Polar
1021 Engineering Conference (ISOPE), Kitakyushu, Japan, May 26-31, 2002.

1022 Timco, G.W., and Frederking, R.M.W. (1990), Compressive Strength of Sea Ice Sheets, Cold Regions Science and
1023 Technology, 17, 227-240.

1024 Timco, G.W., and Johnston, M.E. (2002), Sea Ice Strength during the Melt Season. Proceedings of the 16th
1025 International Association of Hydraulic Engineering and Research (IAHR) International Symposium on Ice,
1026 Dunedin, New Zealand, December 2-6, 2002.

Tonboe, R.T., Dybkjaer, G., and Hoyer, J.L. (2011), Simulations of the snow covered sea ice surface temperature and microwave effective temperature, Tellus, 63A, 1,028-1,037.

Tsonis, A. (2002), An Introduction to Atmospheric Thermodynamics. Cambridge University Press 0-521-79676-8, 182.

Vale (2015), Voisey's Bay. Accessed on the World Wide Web: http://www.vale.com/canada/EN/business/mining/nickel/vale-canada/voiseys-bay/Pages/default.aspx, March 8, 2016.

Water equivalent to snow ratios: DOC/NOAA/NWS (1996), Observing Handbook Number 7, Surface Observations part IV, Supplementary Observations, Table 2-14, 440 pp.

Woods Hole Oceanographic Institute (2010), Humidity, Accessed on the World Wide Web: http://www.whoi.edu/page.do?pid=30578, March 8, 2016.

Yao, T. (2000), Assimilating Sea Surface Temperature Data into an Ice-Ocean Model of the Labrador Sea, Canadian Technical Report of Hydrography and Ocean Sciences, 212.

Yao, T., Tang, C.L., Carrieres, T., and Tran, D.H. (2000a), Verification of a coupled ice ocean forecasting system for the Newfoundland shelf, Atmosphere-Ocean, 38(4), 557-575.

Yao, T., Tang, C.L., and Peterson, I.K. (2000b), Modeling the seasonal variation of sea ice in the Labrador Sea with a coupled multicategory ice model and the Princeton ocean model, Journal of Geophysical Research, 105(C1), 1,153-1,165.